Check for updates

HHO Methods for the Incompressible Navier-Stokes and the Incompressible Euler Equations

Lorenzo Botti[1] · Francesco Carlo Massa[1]

Abstract

We propose two Hybrid High-Order (HHO) methods for the incompressible Navier-Stokes equations and investigate their robustness with respect to the Reynolds number. While both methods rely on a HHO formulation of the viscous term, the pressure-velocity coupling is fundamentally different, up to the point that the two approaches can be considered antithetical. The first method is kinetic energy preserving, meaning that the skew-symmetric discretization of the convective term is guaranteed not to alter the kinetic energy balance. The approximated velocity fields exactly satisfy the divergence free constraint and continuity of the normal component of the velocity is weakly enforced on the mesh skeleton, leading to H-div conformity. The second scheme relies on Godunov fluxes for pressure-velocity coupling: a Harten, Lax and van Leer approximated Riemann Solver designed for cell centered formulations is adapted to hybrid face centered formulations. The resulting numerical scheme is robust up to the inviscid limit, meaning that it can be applied for seeking approximate solutions of the incompressible Euler equations. The schemes are numerically validated performing steady and unsteady two dimensional test cases and evaluating the convergence rates on h-refined mesh sequences. In addition to standard benchmark flow problems, specifically conceived test cases are conducted for studying the error behaviour when approaching the inviscid limit.

✉ Francesco Carlo Massa
  francescocarlo.massa@unibg.it

  Lorenzo Botti
  lorenzo.botti@unibg.it

[1] Dipartimento di Ingegneria e Scienze Applicate, Università degli Studi di Bergamo, viale Marconi 5, 24044 Dalmine, BG, Italy

1 Introduction

In this work we propose and numerically validate two Hybrid High-Order (HHO) methods for the Incompressible Navier-Stokes (INS) equations, governing the flow of incompressible fluids. For the sake of simplicity, we focus on a Newtonian fluid with uniform density. Given a polygonal or polyhedral domain $\Omega \subset \mathbb{R}^d$, $d \in \{2, 3\}$, with boundary $\partial \Omega$, the initial velocity field $\boldsymbol{u}_0 : \Omega \to \mathbb{R}^d$ and a finite time t_F the incompressible Navier-Stokes problem consists in finding the velocity field $\boldsymbol{u} : \Omega \times (0, t_F) \to \mathbb{R}^d$, and the pressure field $p : \Omega \times (0, t_F) \to \mathbb{R}$, such that

$$\frac{\partial \boldsymbol{u}}{\partial t} + \nabla \cdot [(\boldsymbol{u} \otimes \boldsymbol{u}) + p\boldsymbol{I} - \nu \nabla \boldsymbol{u}] = \boldsymbol{f} \qquad \text{in } \Omega \times (0, t_F), \qquad (1a)$$

$$\nabla \cdot \boldsymbol{u} = 0 \qquad \text{in } \Omega \times (0, t_F), \qquad (1b)$$

$$\boldsymbol{u} = \boldsymbol{g}_{\mathrm{D}} \qquad \text{on } \partial \Omega_{\mathrm{D}} \times (0, t_F). \qquad (1c)$$

$$\boldsymbol{n} \cdot [p\boldsymbol{I} - \nu \nabla \boldsymbol{u}] = \boldsymbol{g}_{\mathrm{N}} \qquad \text{on } \partial \Omega_{\mathrm{N}} \times (0, t_F), \qquad (1d)$$

where $\boldsymbol{n}$ denotes the unit vector normal to $\partial \Omega$ pointing out of Ω, ν is the (constant) viscosity, $\boldsymbol{g}_{\mathrm{D}}$ and $\boldsymbol{g}_{\mathrm{N}}$ denote, respectively, the prescribed velocity on the Dirichlet boundary $\partial \Omega_{\mathrm{D}} \subset \partial \Omega$ and the prescribed traction on the Neumann boundary $\partial \Omega_{\mathrm{N}} := \partial \Omega \setminus \partial \Omega_{\mathrm{D}}$, while $\boldsymbol{f} : \Omega \to \mathbb{R}^d$ is a given body force. It is assumed in what follows that both $\partial \Omega_{\mathrm{D}}$ and $\partial \Omega_{\mathrm{N}}$ have non-zero $(d-1)$-dimensional Hausdorff measure (otherwise, additional closure conditions are needed).

HHO methods are gaining momentum in the field of continuum mechanics having been successfully applied to nonlinear elasticity problems [1, 2], diffusion dominated incompressible flow problems [3, 4], porous-media flows [5] and poro-elasticity problems [6, 7]. Similarly to Hybridizable Discontinuous Galerkin (HDG) methods, HHO formulations rely on Degrees Of Freedom (DOFs) associated to polynomial functions defined over mesh elements and mesh faces, the so called elemental and skeletal DOFs. Since solely skeletal DOFs are globally coupled, in particular the face based stencil consist of all mesh faces belonging to the boundary of the two elements sharing the face, elemental degrees of freedom can be eliminated by computing the Schur complement. This procedure is known as *static condensation* and, in this context, *Hybrid* or *Hybridizable* implies that static condensation can be applied to reformulate the problem in terms of skeletal DOFs.

Thanks to static condensations, HHO Jacobian matrices are sparse block matrices whose block size is driven by the dimension of polynomial spaces in $d-1$ variables when considering a d-dimensional flow problem. Accordingly, when accuracy is improved by means of higher-degree p-type expansions, the number of Jacobian matrix non-zero entries grows slower than Discontinuous Galerkin (DG) methods, thereby reducing the computational cost associated to matrix-vector products as well as matrices memory footprint. From the matrix assembly viewpoint HHO methods are generally more expensive than DG methods, also due to the computational cost of static condensation, nevertheless matrix assembly and static condensation are intrinsically parallel tasks that are expected to show optimal scalability on multicore and manycore architectures. Besides computational efficiency considerations, HHO formulations have demonstrated to be robust with respect to mesh distortion and grading [8, 9]. These features are of crucial importance in the context of CFD applications, where boundary layers are commonly employed to improve the resolution near wall.

Since the pioneering works [10–14] dating back to the late 1980s, DG methods have gained increased popularity in computational fluid mechanics, boosted by the 1997 landmark papers [15, 16] on the viscous terms treatment. In the context of incompressible flow problems, stabilized pressure-velocity was proposed by Cockburn *et al.*[17] while Bassi *et al.*[18]

exploited the artificial compressibility idea of Chorin [19] to define suitable Godunov fluxes. Shahbazi *et al.*[20] proposed a semi-explicit time integration with nonlinear terms handled by means of local Lax–Friedrichs fluxes. We also mention segregated approaches employing the Pressure Poisson Equation (PPE) [21, 22]. The extension of DG methods to general polyhedral meshes was theoretically conceived in [23] and [24], leading to adaptive mesh coarsening by agglomeration [25] and high-order accurate geometry representation with arbitrarily coarse meshes [26, 27]. hp-Versions and handling of meshes with small faces have been considered in [28, 29]; see also the recent monograph [30]. More recently, Tavelli and Dumbser [31, 32] and Dumbser *et al.*[33] proposed to use staggered meshes, while Manzanero *et al.*[34] devised an entropy-stable nodal DG spectral element method.

Since the seminal work of Nguyen *et al.*[35], later analyzed by Cesmelioglu *et al.*[36], several HDG discretizations of the incompressible Navier-Stokes equations have been proposed. We mention in particular the *energy stable* and momentum conserving formulation devised by Labeur *et al.*[37] and the superconvergent method by Qiu *et al.*[38]. More recently, Rhebergen *et al.*[39] devised a pointwise divergence free formulation, later analysed by Kirk *et al.*[40]. HHO discretizations of the Navier-Stokes equations have been originally considered in [41, 42]. A kinetic energy preserving formulation was proposed by Botti *et al.*[43], see also [44,Chapters 8 and 9] for further details. Robustness with respect to large irrotational body forces was considered by Castanon *et al.*[45] while extension to non-Newtonian fluids was consedered by Botti *et al.*[46].

In this work, we consider two HHO schemes that are novel variations of existing schemes with improved features. In both cases, the Dirichlet condition on the velocity is enforced weakly in the spirit of [43]. The first scheme, hereafter referred as HHO-Hdiv, borrows the skew-symmetric convective term treatment proposed by Botti *et al.*[43], while the pressure-velocity coupling is inspired by the Hybridizable Discontinuous Galerkin (HDG) method of [39]. Likewise the latter HDG formulation, the method is kinetic energy preserving and yields an exactly divergence free H-div conforming velocity approximation. Pressure-robustness is also guaranteed, meaning that the pressure error does not influence the velocity error. We use polynomials of degree $k + 1$ and k to approximate the velocity and the pressure over mesh elements, respectively. Polynomials of degree $k + 1, k + 1$ and k are employed to approximate the numerical trace of the pressure on mesh faces, velocity on Neumann boundary faces and velocity on internal and Dirichlet boundary faces, respectively. With respect to the HDG formulation of [39], thanks to HHO treatment of the viscous terms in the spirit of [47] (see also [44,Sect. 5.1]), improved orders of convergence are gained on simplicial meshes: in particular we observe $k + 2$ and $k + 1$ convergence rate for the velocity and pressure error in L^2 norm, respectively. Note that the leading block size of the statically condensed Jacobian matrix is driven by skeletal velocity DOFs, mostly associated to polynomials functions of degree k. The second scheme, hereafter referred as HHO-HLL, targets robustness in the inviscid limit. Indeed, as we shall demonstrate by means of numerical test cases, the formulation is able to cope with the incompressible Euler equations. Inspired by DG methods based on Godunov fluxes, see *e.g.,* [18, 48–50] and following the ideas proposed by [51] we employ an Harten, Lax and van Leer (HLL) approximated Riemann solver for designing pressure-velocity coupling and convective term treatment. The scheme relies on polynomials of degree k for both elemental and skeletal unknowns resulting in convergence rates of order $k + 1$ for both the velocity and pressure error in L^2 norm. Moreover, in the diffusion dominated regime, order $k + 2$ for the velocity is recovered. For the reader convenience the most relevant features of the schemes are summarized in Table 1.

The paper is organized as follows. After introducing the discrete settings and the HHO discretization of the viscous term that the two formulations share in common, see Sects. 2.1, 2.2,

Table 1 HHO schemes features

	HHO-Hdiv	HHO-HLL
Pointwise divergence-free	✓	–
Pressure robust	✓	–
Kinetic energy preserving	✓	–
Inviscid limit (Euler eq.)	–	✓
Optimal convergence	✓⋆	✓⁺

Optimal convergence implies a convergence rate of $k + 2$ and $k + 1$ for the velocity and velocity gradient error in L^2 norm, respectively ✓⋆ means that optimal convergence is achieved only on simplicial meshes, ✓⁺ means that optimal convergence is achieved only in the diffusion dominated regime

the `HHO-Hdiv` and `HHO-HLL` formulations of the incompressible Navier-Stokes equations are provided in Sect. 2.4 and 2.5, respectively. Notable features of the proposed formulations are outlined in Sect. 2.4.2, which focus on H-div conformity of `HHO-Hdiv`, and Sect. 2.5.2, which outlines the derivation of the HLL-type Riemann solver which `HHO-HLL` is based upon. In Sect. 3 we tackle several flow configurations, namely Kovasznay flow (Sect. 3.1), LLMS pressure gradient (Sect. 3.2), Gresho-Chan vortex (Sect. 3.3), double shear layer (3.4), and lid-driven cavity flow (Sect. 3.5).

2 Two HHO Methods for the Navier-Stokes Problem

2.1 Discrete Setting

The HHO formulations proposed in this work are capable of dealing with two and three dimensional flow problems. Nevertheless, since numerical test cases focus on two space dimensions, discrete settings are provided for the 2D case. We consider meshes of the domain Ω corresponding to couples $\mathcal{M}_h := (\mathcal{T}_h, \mathcal{F}_h)$, where $\mathcal{T}_h$ is a finite collection of polygonal elements such that $h := \max_{T \in \mathcal{T}_h} h_T > 0$ with h_T denoting the diameter of T, while $\mathcal{F}_h$ is a finite collection of line segments. It is assumed henceforth that the mesh $\mathcal{M}_h$ is shape and contact regular, as detailed in [44,Definition 1.4]. For each mesh element $T \in \mathcal{T}_h$, the faces contained in the element boundary ∂T are collected in the set $\mathcal{F}_T$, and, for each mesh face $F \in \mathcal{F}_h$, $\mathcal{T}_F$ is the set containing the one or two mesh elements sharing F. We define three disjoint subsets of the set $\mathcal{F}_T$: the set of Dirichlet boundary faces $\mathcal{F}_T^D := \{F \in \mathcal{F}_T : F \subset \partial\Omega_D\}$; the set of Neumann boundary faces $\mathcal{F}_T^N := \{F \in \mathcal{F}_T : F \subset \partial\Omega_N\}$; the set of internal faces $\mathcal{F}_T^i := \mathcal{F}_T \setminus (\mathcal{F}_T^D \cup \mathcal{F}_T^N)$. For future use, we also let $\mathcal{F}_T^{i,D} := \mathcal{F}_T^i \cup \mathcal{F}_T^D$. Using the same arguments we define three disjoint subsets of the set $\mathcal{F}_h$: $\mathcal{F}_h^D$, $\mathcal{F}_h^N$, $\mathcal{F}_h^i$ and we let $\mathcal{F}_h^{i,D} := \mathcal{F}_h^i \cup \mathcal{F}_h^D$. For all $T \in \mathcal{T}_h$ and all $F \in \mathcal{F}_T$, $\boldsymbol{n}_{TF}$ denotes the unit vector normal to F pointing out of T.

Hybrid High-Order methods hinge on local polynomial spaces on mesh elements and faces. For given integers $\ell \geq 0$ and $n \geq 1$, we denote by $\mathbb{P}_n^\ell$ the space of n-variate polynomials of total degree $\leq \ell$ (in short, of degree ℓ). For X mesh element or face, we denote by $\mathcal{P}^\ell(X)$ the space spanned by the restriction to X of functions in $\mathbb{P}_d^\ell$. When X is a mesh face, the resulting space is isomorphic to $\mathbb{P}_{d-1}^\ell$ (see [44,Proposition 1.23]).

Let again X denote a mesh element or face. The local L^2-orthogonal projector $\pi_X^\ell :$ $L^2(X) \to \mathcal{P}^\ell(X)$ is such that, for all $q \in L^2(X)$,

$$\int_X (q - \pi_X^\ell q) r = 0 \quad \forall r \in \mathcal{P}^\ell(X).$$

Notice that, above and in what follows, we omit the measure from integrals as it can always be inferred from the context. The L^2-orthogonal projector on $\mathcal{P}^\ell(X)^d$, obtained applying π_X^ℓ component-wise, is denoted by $\boldsymbol{\pi}_X^\ell$.

2.2 HHO Discretization of the Laplace Operator

The HHO discretizations of the Navier-Stokes problem considered in this work hinge on velocity reconstructions devised at the element level and obtained assembling diffusive potential reconstructions component-wise. In what follows, we let a mesh element $T \in \mathcal{T}_h$ be fixed, denote by $k \geq 0$ the degree of polynomials attached to internal and Dirichlet mesh faces, by $t \in \{k, k+1\}$ the degree of polynomials attached to mesh elements and by $f \in \{k, k+1\}$ the degree of polynomials attached to Neumann faces. We remark that, the motivation for choosing t and f one degree higher than k will be given in Sect. 2.4.2.

2.2.1 Scalar Potential Reconstruction

The velocity reconstruction is obtained leveraging, for each component, the *scalar potential reconstruction* originally introduced in [52] in the context of scalar diffusion problems (see also [47] and [44,Sect. 5.1] for its generalization to the case of different polynomial degrees on elements and faces). Define the local scalar HHO space

$$\underline{V}_T^{t,k,f} := \left\{ \underline{v}_T = \left(v_T, (v_F)_{F \in \mathcal{F}_T}\right) : \begin{array}{l} v_T \in \mathcal{P}^t(T), \\ v_F \in \mathcal{P}^k(F) \text{ for all } F \in \mathcal{F}_T^{\mathrm{i,D}}, \\ v_F \in \mathcal{P}^f(F) \text{ for all } F \in \mathcal{F}_T^{\mathrm{N}} \end{array} \right\}. \tag{2}$$

The scalar potential reconstruction operator $\mathfrak{p}_T^{k+1} : \underline{V}_T^{t,k,f} \to \mathcal{P}^{k+1}(T)$ maps a vector of polynomials of $\underline{V}_T^{t,k,f}$ onto a polynomial of degree $(k+1)$ over T as follows: Given $\underline{v}_T \in \underline{V}_T^{t,k,f}$, $\mathfrak{p}_T^{k+1}\underline{v}_T$ is the unique polynomial in $\mathcal{P}^{k+1}(T)$ satisfying $\forall w_T \in \mathcal{P}^{k+1}(T)$,

$$\int_T \nabla \mathfrak{p}_T^{k+1} \underline{v}_T \cdot \nabla w_T = \int_T \nabla v_T \cdot \nabla w_T + \sum_{F \in \mathcal{F}_T} \int_F (v_F - v_T) \, \nabla w_T \cdot \boldsymbol{n}_{TF}$$

$$\int_T \mathfrak{p}_T^{k+1} \underline{v}_T = \int_T v_T.$$

Computing $\mathfrak{p}_T^{k+1}$ for each $T \in \mathcal{T}_h$ requires to solve a small linear system. This task shows optimal scalability on parallel architectures and is performed using a Cholesky factorization.

2.2.2 Velocity Reconstruction

Define, in analogy with (2), the following vector-valued HHO space for the velocity:

$$\underline{\boldsymbol{V}}_T^{t,k,f} := \left\{ \underline{\boldsymbol{v}}_T = (\boldsymbol{v}_T, (\boldsymbol{v}_F)_{F \in \mathcal{F}_T}) : \begin{array}{l} \boldsymbol{v}_T \in \mathcal{P}^t(T)^d, \\ \boldsymbol{v}_F \in \mathcal{P}^k(F)^d \text{ for all } F \in \mathcal{F}_T^{\mathrm{i,D}}, \\ \boldsymbol{v}_F \in \mathcal{P}^f(F)^d \text{ for all } F \in \mathcal{F}_T^{\mathrm{N}} \end{array} \right\}. \tag{3}$$

The *velocity reconstruction* $\mathfrak{P}_T^{k+1} : \underline{V}_T^{t,k,f} \to \mathcal{P}^{k+1}(T)^d$ is obtained setting

$$\mathfrak{P}_T^{k+1} \underline{v}_T := \left(\mathfrak{p}_T^{k+1} \underline{v}_{T,i} \right)_{i=1,\ldots,d},$$

where, for all $i = 1, \ldots, d$, $\underline{v}_{T,i} \in \underline{V}_T^{t,k,f}$ is obtained gathering the ith components of the polynomials in $\underline{v}_T$, i.e., $\underline{v}_{T,i} := \left(v_{T,i}, (v_{F,i})_{F \in \mathcal{F}_T} \right)$ if $v_T = (v_{T,i})_{i=1,\ldots,d}$ and $v_F = (v_{F,i})_{i=1,\ldots,d}$ for all $F \in \mathcal{F}_T$.

The local interpolation operator $\underline{I}_T^{t,k,f} : H^1(T)^d \to \underline{V}_T^{t,k,f}$ is defined as follows: For all $v \in H^1(T)^d$,

$$\underline{I}_T^{t,k,f} v := \left(\boldsymbol{\pi}_T^t v, (\boldsymbol{\pi}_F^k v_{|F})_{F \in \mathcal{F}_T^{i,D}}, (\boldsymbol{\pi}_F^f v_{|F})_{F \in \mathcal{F}_T^N} \right). \tag{4}$$

Following [44,Sect. 5.1.3], it is possible to demonstrate that the velocity reconstruction is such that, for all $v \in H^1(T)^d$

$$\int_T \left(\nabla \mathfrak{P}_T^{k+1} \underline{I}_T^{t,k,f} v - \nabla v \right) : \nabla w_T = 0 \text{ for all } w_T \in \mathcal{P}^{k+1}(T)^d \text{ and } \int_T \mathfrak{P}_T^{k+1} \underline{I}_T^{t,k,f} v = \int_T v. \tag{5}$$

The above result is of crucial importance for inferring the approximation properties of the velocity reconstruction operator.

2.2.3 Face Residuals

Let $T \in \mathcal{T}_h$ and $F \in \mathcal{F}_T$. The stabilization bilinear form for the HHO discretization of the viscous term in the momentum equation (1a) hinges on the residual operator $\mathfrak{r}_{TF}^k : \underline{V}_T^{t,k,f} \to \underline{V}_T^{t,k,f}$ defined as follows

$$\mathfrak{r}_{TF}^k \underline{v}_T := \mathfrak{r}_F^{k,f} \underline{v}_T - \mathfrak{r}_T^t \underline{v}_T$$

where the *face residual* $\mathfrak{r}_F^{k,f} : \underline{V}_T^{t,k,f} \to \mathcal{P}^{k,f}(F)$ and the *element residual* $\mathfrak{r}_T^t : \underline{V}_T^{t,k,f} \to \mathcal{P}^t(T)$ such that, for all $\underline{v}_T \in \underline{V}_T^{t,k,f}$,

$$\mathfrak{r}_F^{k,f} \underline{v}_T := \begin{cases} \pi_F^k \left(v_F - \mathfrak{p}_T^{k+1} \underline{v}_T \right) & \text{if } F \in \mathcal{F}_h^{i,D} \\ \pi_F^f \left(v_F - \mathfrak{p}_T^{k+1} \underline{v}_T \right) & \text{if } F \in \mathcal{F}_h^N \end{cases} \quad \text{and} \quad \mathfrak{r}_T^t \underline{v}_T =:= \pi_T^t \left(v_T - \mathfrak{p}_T^{k+1} \underline{v}_T \right).$$

The vector residual $\mathfrak{R}_{TF}^k : \underline{V}_T^{t,k,f} \to \underline{V}_T^{t,k,f}$ is such that, for all $\underline{v}_T \in \underline{V}_T^{t,k,f}$:

$$\mathfrak{R}_{TF}^k \underline{v}_T := \left(\mathfrak{r}_{TF}^k \underline{v}_{T,i} \right)_{i=1,\ldots,d}.$$

2.3 Local and Global HHO Spaces for Velocity and Pressure Unknowns

In addition to the scalar and vector valued local velocity spaces $\underline{V}_T^{t,k,f}$ and $\underline{V}_T^{t,k,f}$ defined in (2) and (3), respectively, we need to introduce local pressure spaces and global HHO spaces for both velocity and pressure.

Let $T \in \mathcal{T}_h$ and define the local HHO space for the pressure unknown

$$\underline{Q}_T^{k,p} := \left\{ \underline{q}_T = \left(q_T, (q_F)_{F \in \mathcal{F}_T} \right) : q_T \in \mathcal{P}^k(T) \text{ and } q_F \in \mathcal{P}^p(F) \text{ for all } F \in \mathcal{F}_T \right\}, \tag{6}$$

where $p \in \{k, k+1\}$. The global HHO space for the pressure unknown is defined as follows

$$\underline{Q}_h^{k,p} := \left\{ \underline{q}_h = ((q_T)_{T \in \mathcal{T}_h}, (q_F)_{F \in \mathcal{F}_h}) : \begin{array}{l} q_T \in \mathcal{P}^k(T) \text{ for all } T \in \mathcal{T}_h \\ q_F \in \mathcal{P}^p(F) \text{ for all } F \in \mathcal{F}_h. \end{array} \right\}$$

For all $\underline{q}_h \in \underline{Q}_h^{k,p}$ and all $T \in \mathcal{T}_h$, we denote by $\underline{q}_T \in \underline{Q}_T^{k,p}$ the restriction of $\underline{q}_h$ to T.
    To conclude, the global HHO space for the velocity unknown reads

$$
\underline{V}_h^{t,k,f} := \left\{ \underline{v}_h = ((v_T)_{T \in \mathcal{T}_h}, (v_F)_{F \in \mathcal{F}_h}) : \begin{array}{l} v_T \in \mathcal{P}^t(T)^d \text{ for all } T \in \mathcal{T}_h, \\ v_F \in \mathcal{P}^k(F)^d \text{ for all } F \in \mathcal{F}_h^{i,D}, \\ v_F \in \mathcal{P}^f(F)^d \text{ for all } F \in \mathcal{F}_h^{N} \end{array} \right\}.
$$

For all $\underline{v}_h \in \underline{V}_h^{t,k,f}$ and all $T \in \mathcal{T}_h$, we denote by $\underline{v}_T \in \underline{V}_T^{t,k,f}$ the restriction of $\underline{v}_h$ to T.

2.4 A Pointwise Divergence Free H-div Conforming HHO Scheme

2.4.1 Local and Global Residuals

We combine the HHO discretization of the viscous term with a hybrid approximation of the pressure inspired by [39]. Given $(\underline{u}_T, \underline{p}_T) \in \underline{V}_T^{t,k,f} \times \underline{Q}_T^{k,p}$, the local residuals $r_{I,T}^{\text{mnt}}((\underline{u}_T, \underline{p}_T); \cdot) : \underline{V}_T^{t,k,f} \to \mathbb{R}$ of the space discrete momentum and $r_{I,T}^{\text{cnt}}(\underline{u}_T; \cdot) : \underline{Q}_T^{k,p} \to \mathbb{R}$ of the discrete mass conservation equations are such that, for all $\underline{v}_T \in \underline{V}_T^{t,k,f}$ and all $\underline{q}_T \in \underline{Q}_T^{k,p}$,

$$
r_{I,T}^{\text{mnt}}((\underline{u}_T, \underline{p}_T); \underline{v}_T) :=
$$

$$
\underbrace{\int_T \left(\frac{\partial u_T}{\partial t} - f \right) \cdot v_T + \int_T \nu \nabla \mathfrak{P}_T^{k+1} \underline{u}_T : \nabla \mathfrak{P}_T^{k+1} \underline{v}_T + \sum_{F \in \mathcal{F}_T} \frac{\nu}{h_F} \int_F \mathfrak{R}_{TF}^k \underline{v}_T \cdot \mathfrak{R}_{TF}^k \underline{v}_T}_{\text{viscous term discretization, see Sect. 2.2}}
$$

$$
+ \underbrace{\sum_{F \in \mathcal{F}_T^D} \int_F \left[\left(-n_{TF} \cdot \nu \nabla \mathfrak{P}_T^{k+1} \underline{u}_T \right) \cdot v_F + (u_F - g_D) \cdot \left(n_{TF} \cdot \nu \nabla \mathfrak{P}_T^{k+1} \underline{v}_T \right) \right] + \sum_{F \in \mathcal{F}_T^D} \frac{\eta \nu}{h_F} \int_F (u_F - g_D) \cdot v_F}_{\text{viscous term discretization (weak imposition of Dirichlet boundary conditions), see [43, Remark 6]}}
$$

$$
+ \underbrace{\frac{1}{2} \left(\int_T (u_T \cdot \nabla u_T) \cdot v_T - \int_T (u_T \otimes u_T) : \nabla v_T + \sum_{F \in \mathcal{F}_T} \int_F (u_F \cdot n_{TF})(u_F \cdot v_T - u_T \cdot v_F) \right)}_{\text{convective trilinear term discretization, see [43]}}
$$

$$
+ \underbrace{\frac{1}{2} \left(\sum_{F \in \mathcal{F}_T^D} \int_F (u_F \cdot n_{TF}) g_D \cdot v_F + \sum_{F \in \mathcal{F}_T^N} \int_F (u_F \cdot n_{TF}) u_T \cdot v_F \right)}_{\text{convective trilinear term discretization (boundary conditions), see [43]}} - \underbrace{\sum_{F \in \mathcal{F}_T^N} \int_F g_N \cdot v_F}_{\text{Neumann BCs}}
$$

$$
\underbrace{- \int_T p_T (\nabla \cdot v_T) + \sum_{F \in \mathcal{F}_T} \int_F p_F (v_T - v_F) \cdot n_{TF} + \sum_{F \in \mathcal{F}_T^D} \int_F p_F (v_F \cdot n_{TF})}_{\text{pressure-velocity coupling discretization, see Sect. 2.4.2}},
$$

$$
r_{I,T}^{\text{cnt}}(\underline{u}_T; \underline{q}_T) :=
$$

$$
\underbrace{- \int_T (\nabla \cdot u_T) q_T + \sum_{F \in \mathcal{F}_T} \int_F (u_T - u_F) \cdot n_{TF} q_F + \sum_{F \in \mathcal{F}_T^D} \int_F (u_F - g_D) \cdot n_{TF} q_F}_{\text{pressure-velocity coupling discretization, see Sect. 2.4.2}}.
$$

In the expression of $r_{I,T}^{\text{mnt}}((\underline{u}_T, \underline{p}_T); \cdot)$, $\eta > 0$ is required to ensure coercivity, see [43,Remark 6] for details. The penalty term where the parameter η appears, along with the consistency terms in the second line, are responsible for the weak enforcement of Dirichlet boundary conditions for the velocity. In the numerical tests provided below, η is taken

equal to 3. This choice leads to small but perceivable accuracy improvements as compared with η equal to one.

The global residuals $r_{I,h}^{\text{mnt}}((\underline{\boldsymbol{u}}_h, \underline{p}_h); \cdot) : \underline{\boldsymbol{V}}_h^{t,k,f} \to \mathbb{R}$ and $r_{I,h}^{\text{cnt}}(\underline{\boldsymbol{u}}_h; \cdot) : \underline{Q}_h^{k,p} \to \mathbb{R}$ are obtained by element-by-element assembly of the local residuals, *i.e.*: For all $\underline{\boldsymbol{v}}_h \in \underline{\boldsymbol{V}}_h^{t,k,f}$ and all $\underline{q}_h \in \underline{Q}_h^{k,p}$,

$$r_{I,h}^{\text{mnt}}\left((\underline{\boldsymbol{u}}_h, \underline{p}_h); \underline{\boldsymbol{v}}_h\right) := \sum_{T \in \mathcal{T}_h} r_{I,T}^{\text{mnt}}\left((\underline{\boldsymbol{u}}_T, \underline{p}_T); \underline{\boldsymbol{v}}_T\right),$$

$$r_{I,h}^{\text{cnt}}(\underline{\boldsymbol{u}}_h; \underline{q}_h) := \sum_{T \in \mathcal{T}_h} r_{I,T}^{\text{cnt}}(\underline{\boldsymbol{u}}_T; \underline{q}_T). \tag{8}$$

The HHO scheme with pointwise divergence free H-div conforming velocity field is obtained setting the polynomial degrees as $t = f = p = k + 1$.

Scheme 1 (HHO-Hdiv) Find $(\underline{\boldsymbol{u}}_h, \underline{p}_h) \in \underline{\boldsymbol{V}}_h^{k+1,k,k+1} \times \underline{Q}_h^{k,k+1}$ such that

$$\begin{aligned} r_{I,h}^{\text{mnt}}((\underline{\boldsymbol{u}}_h, \underline{p}_h); \underline{\boldsymbol{v}}_h) &= 0 & \forall \underline{\boldsymbol{v}}_h &\in \underline{\boldsymbol{V}}_h^{k+1,k,k+1}, \\ r_{I,h}^{\text{cnt}}(\underline{\boldsymbol{u}}_h; \underline{q}_h) &= 0 & \forall \underline{q}_h &\in \underline{Q}_h^{k,k+1}. \end{aligned} \tag{9}$$

2.4.2 Discrete Mass Conservation and H-div Conformity

For each $\underline{\boldsymbol{u}}_h \in \underline{\boldsymbol{V}}_h^{t,k,f}$, $r_{I,h}^{\text{cnt}} = 0$ for all $\underline{q}_h \in \underline{Q}_h^{k,p}$ implies that

1. if $q_F = 0$ for all $F \in \mathcal{F}_h$, then $\int_T (\nabla \cdot \boldsymbol{u}_T) q_T = 0$, for each $T \in \mathcal{T}_h$;
2. if $q_T = 0$ for all $T \in \mathcal{T}_h$, then

$$\begin{cases} \int_F (\boldsymbol{u}_T - \boldsymbol{u}_{T'}) \cdot \boldsymbol{n}_{TF} \, q_F = 0, & \text{for each } F \in \mathcal{F}_T^{\text{i}} \cap \mathcal{F}_{T'}^{\text{i}} \text{ with } T, T' \in \mathcal{T}_h, T \neq T'; \\ \int_F (\boldsymbol{u}_T - \boldsymbol{u}_F) \cdot \boldsymbol{n}_{TF} \, q_F = 0, & \text{for each } T \in \mathcal{T}_h, F \in \mathcal{F}_T^{\text{N}}; \\ \int_F (\boldsymbol{u}_T - \boldsymbol{g}_{\text{D}}) \cdot \boldsymbol{n}_{TF} \, q_F = 0, & \text{for each } T \in \mathcal{T}_h, F \in \mathcal{F}_T^{\text{D}}. \end{cases}$$

Setting $t = f = p = k + 1$, it is straightforward to conclude that

$$\nabla \cdot \boldsymbol{u}_T = 0, \quad \forall \boldsymbol{x} \in T, \quad \forall T \in \mathcal{T}_h; \tag{10}$$

$$(\boldsymbol{u}_T - \boldsymbol{u}_{T'}) \cdot \boldsymbol{n}_{TF} = 0, \quad \forall \boldsymbol{x} \in F, \quad \text{for each } F \in \mathcal{F}_T^{\text{i}} \cap \mathcal{F}_{T'}^{\text{i}} \text{ with } T, T' \in \mathcal{T}_h, T \neq T'; \tag{11}$$

$$(\boldsymbol{u}_T - \boldsymbol{u}_F) \cdot \boldsymbol{n}_{TF} = 0, \quad \forall \boldsymbol{x} \in F, \quad \text{for each } T \in \mathcal{T}_h, F \in \mathcal{F}_T^{\text{N}}; \tag{12}$$

$$(\boldsymbol{u}_T - \boldsymbol{\pi}_F^{k+1} \boldsymbol{g}_{\text{D}}) \cdot \boldsymbol{n}_{TF} = 0, \quad \forall \boldsymbol{x} \in F, \quad \text{for each } T \in \mathcal{T}_h, F \in \mathcal{F}_T^{\text{D}}. \tag{13}$$

Remark 1 (Polynomial degree of velocity unknowns over Neumann faces) When $t = p = k + 1$, choosing $f = k + 1$ is mandatory to ensure H-div conformity on Neumann faces without constraining velocity unknowns over mesh elements. Note in particular that setting $f = k$ would imply that, according to (12), $\boldsymbol{u}_T|_F \in \mathcal{P}^k(F)$ for each $F \in \mathcal{F}_h^{\text{N}}$. We also remark that setting $f = k$ is perfectly fine if $\boldsymbol{g}_{\text{N}}$ is a constant, in particular traction-free boundary conditions commonly employed on outflow sections of channel flows can be dealt with without raising the polynomial degree on outflow faces.

Remark 2 (*h*-Convergence rates on simplicial and general meshes) The `HHO-Hdiv` formulations show convergence rates of order $k + 1$ for the pressure error in L^2 norm on both simplicial and general meshes. Convergence rates of order $k + 2$ and $k + 1$ for the velocity and velocity gradients error in L^2 norm, respectively, are attained on simplicial meshes, while, on general meshes, convergence rates are reduced by one order. Choosing $t = k + 1$ and $f = p = k$ allows to recover optimal convergence rates for the velocity on general meshes but H-div conformity and pressure-robustness are lost. Indeed, (11)-(12)-(13) are replaced by the following looser conditions on the normal trace of the velocity

$$(\pi_F^k \boldsymbol{u}_T - \pi_F^k \boldsymbol{u}_{T'}) \cdot \boldsymbol{n}_{TF} = 0, \quad \forall \boldsymbol{x} \in F, \quad \text{for each } F \in \mathcal{F}_T^{\mathrm{i}} \cap \mathcal{F}_{T'}^{\mathrm{i}} \text{ with } T, T' \in \mathcal{T}_h, T \neq T'; \tag{14}$$

$$(\pi_F^k \boldsymbol{u}_T - \boldsymbol{u}_F) \cdot \boldsymbol{n}_{TF} = 0, \quad \forall \boldsymbol{x} \in F, \quad \text{for each } T \in \mathcal{T}_h, F \in \mathcal{F}_T^{\mathrm{N}} \tag{15}$$

$$(\pi_F^k \boldsymbol{u}_T - \pi_F^k \boldsymbol{g}_{\mathrm{D}}) \cdot \boldsymbol{n}_{TF} = 0, \quad \forall \boldsymbol{x} \in F, \quad \text{for each } T \in \mathcal{T}_h, F \in \mathcal{F}_T^{\mathrm{D}} \tag{16}$$

Since (10) holds, the method yields a pointwise divergence free velocity field. The HHO scheme with pointwise divergence free velocity and optimal convergence properties on general meshes is outlined in what follows for the sake of completeness.

Scheme 2 (`HHO-DivFree`) Find $(\underline{\boldsymbol{u}}_h, \underline{p}_h) \in \underline{\boldsymbol{V}}_h^{k+1,k,k} \times \underline{Q}_h^{k,k}$ such that

$$\begin{aligned} r_{I,h}^{\mathrm{mnt}}((\underline{\boldsymbol{u}}_h, \underline{p}_h); \underline{\boldsymbol{v}}_h) = 0 &\qquad \forall \underline{\boldsymbol{v}}_h \in \underline{\boldsymbol{V}}_h^{k+1,k,k+1}, \\ r_{I,h}^{\mathrm{cnt}}(\underline{\boldsymbol{u}}_h; \underline{q}_h) = 0 &\qquad \forall \underline{q}_h \in \underline{Q}_h^{k,k+1}. \end{aligned} \tag{17}$$

2.5 A HHO Formulation Robust in the Inviscid Limit

2.5.1 Local and Global Residuals

Given $(\underline{\boldsymbol{u}}_T, \underline{p}_T) \in \underline{\boldsymbol{V}}_T^{t,k,f} \times \underline{Q}_T^{k,p}$, the local residuals $r_{II,T}^{\mathrm{mnt}}((\underline{\boldsymbol{u}}_T, \underline{p}_T); \cdot) : \underline{\boldsymbol{V}}_T^{t,k,f} \to \mathbb{R}$ of the space discrete momentum and $r_{II,T}^{\mathrm{cnt}}(\underline{\boldsymbol{u}}_T; \cdot) : \underline{Q}_T^{k,p} \to \mathbb{R}$ of the discrete mass conservation equations are such that, for all $\underline{\boldsymbol{v}}_T \in \underline{\boldsymbol{V}}_T^{t,k,f}$ and all $\underline{q}_T \in \underline{Q}_T^{k,p}$,

$$r_{II,T}^{\mathrm{mnt}}((\underline{\boldsymbol{u}}_T, \underline{p}_T); \underline{\boldsymbol{v}}_T) :=$$

$$\underbrace{\int_T \left(\frac{\partial \boldsymbol{u}_T}{\partial t} - \boldsymbol{f}\right) \cdot \boldsymbol{v}_T + \int_T \nu \nabla \mathfrak{P}_T^{k+1} \underline{\boldsymbol{u}}_T : \nabla \mathfrak{P}_T^{k+1} \underline{\boldsymbol{v}}_T + \sum_{F \in \mathcal{F}_T} \frac{\nu}{h_F} \int_F \mathfrak{R}_{TF}^k \underline{\boldsymbol{v}}_T \cdot \mathfrak{R}_{TF}^k \underline{\boldsymbol{v}}_T}_{\text{viscous term discretization, see Sect. 2.2}}$$

$$\underbrace{+ \sum_{F \in \mathcal{F}_T^{\mathrm{D}}} \int_F \left[(-\boldsymbol{n}_{TF} \cdot \nu \nabla \mathfrak{P}_T^{k+1} \underline{\boldsymbol{u}}_T) \cdot \boldsymbol{v}_F + (\boldsymbol{u}_F - \boldsymbol{g}_{\mathrm{D}}) \cdot (\boldsymbol{n}_{TF} \cdot \nu \nabla \mathfrak{P}_T^{k+1} \underline{\boldsymbol{v}}_T)\right] + \sum_{F \in \mathcal{F}_T^{\mathrm{D}}} \frac{\eta \nu}{h_F} \int_F (\boldsymbol{u}_F - \boldsymbol{g}_{\mathrm{D}}) \cdot \boldsymbol{v}_F}_{\text{viscous term discretization (weak imposition of Dirichlet boundary conditions), see [43, Remark 6]}}$$

$$\underbrace{- \int_T (\boldsymbol{u}_T \otimes \boldsymbol{u}_T) : \nabla \boldsymbol{v}_T + \sum_{F \in \mathcal{F}_T} \int_F (\boldsymbol{u}_F \cdot \boldsymbol{n}_{TF}) \boldsymbol{u}_F \cdot \boldsymbol{v}_T + \sum_{F \in \mathcal{F}_T} \int_F s^+(\boldsymbol{u}_T - \boldsymbol{u}_F) \cdot (\boldsymbol{v}_T - \boldsymbol{v}_F)}_{\text{convective trilinear term discretization, see Sect. 2.5.2}}$$

$$\underbrace{- \int_T p_T (\nabla \cdot \boldsymbol{v}_T) + \sum_{F \in \mathcal{F}_T} \int_F p_F (\boldsymbol{v}_T \cdot \boldsymbol{n}_{TF})}_{\text{pressure-velocity coupling, see Sect. 2.5.2}} + \underbrace{\sum_{F \in \mathcal{F}_T^{\mathrm{D}}} \int_F s^-(\boldsymbol{g}_{\mathrm{D}} - \boldsymbol{u}_F) \cdot \boldsymbol{v}_F}_{\text{convective trilinear term (Dirichlet BCs)}} - \underbrace{\sum_{F \in \mathcal{F}_T^{\mathrm{N}}} \int_F (\boldsymbol{g}_{\mathrm{N}} - p_F \boldsymbol{n}_{TF}) \cdot \boldsymbol{v}_F,}_{\text{Neumann BCs (viscous contribution)}}$$

$$r_{II,T}^{\mathrm{cnt}}(\underline{\boldsymbol{u}}_T; \underline{q}_T) :=$$

$$\underbrace{-\int_T \boldsymbol{u}_T \cdot \nabla q_T + \sum_{F \in \mathcal{F}_T} \int_F \boldsymbol{u}_F \cdot \boldsymbol{n}_{TF}\, q_T + \sum_{F \in \mathcal{F}_T} \int_F \frac{s^+}{a^2}(p_T - p_F)(q_T - q_F)}_{\text{pressure-velocity coupling, see Sect. 2.5.2}}$$

$$\underbrace{+ \sum_{F \in \mathcal{F}_T^{\mathrm{N}}} \int_F \frac{s^-}{a^2}\left((\boldsymbol{g}_{\mathrm{N}} + \boldsymbol{n}_{TF} \cdot \nu \nabla \mathfrak{P}_T^{k+1} \boldsymbol{u}_T) \cdot \boldsymbol{n}_{TF} - p_F\right) q_F,}_{\text{Neumann boundary conditions (inviscid contribution)}}$$

where

$$s^\pm = \frac{1}{2}\left(\boldsymbol{u}_F \cdot \boldsymbol{n}_{TF} \pm \sqrt{(\boldsymbol{u}_F \cdot \boldsymbol{n}_{TF})^2 + 4a^2}\right) \tag{19}$$

and a is the artificial compressibility parameter. In the numerical tests provided below, a is taken as a unit velocity. In the expression of $r_{II,T}^{\mathrm{mnt}}((\underline{\boldsymbol{u}}_T, \underline{p}_T); \cdot)$, $\eta > 0$ is required to ensure coercivity, see [43][Remark 6] for details. In the numerical tests provided below, η is taken equal to 3. This choice leads to small but perceivable accuracy improvements as compared with η equal to one.

The global residuals $r_{II,h}^{\mathrm{mnt}}((\underline{\boldsymbol{u}}_h, \underline{p}_h); \cdot) : \underline{\boldsymbol{V}}_h^{t,k,f} \to \mathbb{R}$ and $r_{II,h}^{\mathrm{cnt}}(\underline{\boldsymbol{u}}_h; \cdot) : \underline{Q}_h^{k,p} \to \mathbb{R}$ are obtained by element-by-element assembly of the local residuals, *i.e.*: For all $\underline{\boldsymbol{v}}_h \in \underline{\boldsymbol{V}}_h^{t,k,f}$ and all $\underline{q}_h \in \underline{Q}_h^{k,p}$,

$$r_{II,h}^{\mathrm{mnt}}\left((\underline{\boldsymbol{u}}_h, \underline{p}_h); \underline{\boldsymbol{v}}_h\right) := \sum_{T \in \mathcal{T}_h} r_{II,T}^{\mathrm{mnt}}\left((\underline{\boldsymbol{u}}_T, \underline{p}_T); \underline{\boldsymbol{v}}_T\right),$$

$$r_{II,h}^{\mathrm{cnt}}(\underline{\boldsymbol{u}}_h; \underline{q}_h) := \sum_{T \in \mathcal{T}_h} r_{II,T}^{\mathrm{cnt}}(\underline{\boldsymbol{u}}_T; \underline{q}_T). \tag{20}$$

The HHO scheme based on the HLL Riemann solver is obtained setting the polynomial degrees as $t = f = p = k$.

Scheme 3 (HHO-HLL) Find $(\underline{\boldsymbol{u}}_h, \underline{p}_h) \in \underline{\boldsymbol{V}}_h^{k,k,k} \times \underline{Q}_h^{k,k}$ such that

$$\begin{aligned} r_{II,h}^{\mathrm{mnt}}((\underline{\boldsymbol{u}}_h, \underline{p}_h); \underline{\boldsymbol{v}}_h) = 0 &\qquad \forall \underline{\boldsymbol{v}}_h \in \underline{\boldsymbol{V}}_h^{k,k,k}, \\ r_{II,h}^{\mathrm{cnt}}(\underline{\boldsymbol{u}}_h; \underline{q}_h) = 0 &\qquad \forall \underline{q}_h \in \underline{Q}_h^{k,k}. \end{aligned} \tag{21}$$

2.5.2 Artificial Compressibility Based HLL-type Numerical Flux

In order to outline the convective term and pressure-velocity coupling formulations we focus on the inviscid framework and, for the sake of conciseness, we assume that periodic boundary conditions are imposed over $\partial\Omega$. Accordingly, the local residuals for the HHO-HLL discretization of the Euler equations on a periodic domain reads: given $(\underline{\boldsymbol{u}}_T, \underline{p}_T) \in \underline{\boldsymbol{V}}_T^{k,k,k} \times \underline{Q}_T^{k,k}$, for all $\underline{\boldsymbol{v}}_T \in \underline{\boldsymbol{V}}_T^{k,k,k}$ and all $\underline{q}_T \in \underline{Q}_T^{k,k}$

$$\begin{aligned} r_{II,T}^{\mathrm{mnt}}((\underline{\boldsymbol{u}}_T, \underline{p}_T); \underline{\boldsymbol{v}}_T) = &\int_T (\boldsymbol{u}_T \otimes \boldsymbol{u}_T + p_T \boldsymbol{I}) : \nabla \boldsymbol{v}_T + \int_T \left(\frac{\partial \boldsymbol{u}_T}{\partial t} - \boldsymbol{f}\right) \cdot \boldsymbol{v}_T \\ &+ \sum_{F \in \mathcal{F}_T} \int_F \left[(\boldsymbol{u}_F \otimes \boldsymbol{u}_F + p_F \boldsymbol{I}) \cdot \boldsymbol{n}_{TF} + s^+(\boldsymbol{u}_T - \boldsymbol{u}_F)\right] \cdot (\boldsymbol{v}_T - \boldsymbol{v}_F), \end{aligned} \tag{22}$$

$$r_{II,T}^{\mathrm{cnt}}(\underline{\boldsymbol{u}}_T; \underline{q}_T) = -\int_T \boldsymbol{u}_T \cdot \nabla q_T + \sum_{F \in \mathcal{F}_T} \int_F \left[\boldsymbol{u}_F \cdot \boldsymbol{n}_{TF} + \frac{s^+}{a^2}(p_T - p_F)\right](q_T - q_F). \tag{23}$$

The terms within square brackets are the, so called, *numerical fluxes* of the HHO formulation.

In order to outline the trace conditions enforced over mesh faces we now consider the global residuals of the Euler equations with Dirichlet and Neumann boundary conditions imposed over $\partial\Omega$. For each $(\underline{\boldsymbol{u}}_h, \underline{p}_h) \in \underline{\boldsymbol{V}}_h^{k,k,k} \times \underline{Q}_h^{k,k}$, $r_{II,h}^{\mathrm{mnt}} = 0$ for all $\boldsymbol{v}_h \in \underline{\boldsymbol{V}}_h^{k,k,k}$ such that $\boldsymbol{v}_T = 0$ for all $T \in \mathcal{T}_h$, implies that

$$\int_F \left[s^+(\boldsymbol{u}_T - \boldsymbol{u}_F) - s^-(\boldsymbol{u}_{T'} - \boldsymbol{u}_F) \right] \cdot \boldsymbol{v}_F = 0, \qquad \text{for each } F \in \mathcal{F}_T^{\mathrm{i}} \cap \mathcal{F}_{T'}^{\mathrm{i}} \text{ with } T, T' \in \mathcal{T}_h, T \neq T';$$

$$\int_F s^+(\boldsymbol{u}_T - \boldsymbol{u}_F) \cdot \boldsymbol{v}_F = 0, \qquad \text{for each } T \in \mathcal{T}_h, F \in \mathcal{F}_T^{\mathrm{N}};$$

$$\int_F \left[s^+(\boldsymbol{u}_T - \boldsymbol{u}_F) - s^-(\boldsymbol{g}_{\mathrm{D}} - \boldsymbol{u}_F) \right] \cdot \boldsymbol{v}_F = 0, \qquad \text{for each } T \in \mathcal{T}_h, F \in \mathcal{F}_T^{\mathrm{D}}.$$

For each $\underline{\boldsymbol{u}}_h \in \underline{\boldsymbol{V}}_h^{k,k,k}$, $r_{II,h}^{\mathrm{cnt}} = 0$ for all $\underline{q}_h \in \underline{Q}_h^{k,k}$ such that $q_T = 0$ for all $T \in \mathcal{T}_h$, implies that

$$\int_F \left[s^+(p_T - p_F) - s^-(p_{T'} - p_F) \right] q_F = 0, \qquad \text{for each } F \in \mathcal{F}_T^{\mathrm{i}} \cap \mathcal{F}_{T'}^{\mathrm{i}} \text{ with } T, T' \in \mathcal{T}_h, T \neq T';$$

$$\int_F \left[s^+(p_T - p_F) - s^- \left(\boldsymbol{g}_{\mathrm{N}} \cdot \boldsymbol{n}_{TF} - p_F \right) \right] q_F = 0, \qquad \text{for each } T \in \mathcal{T}_h, F \in \mathcal{F}_T^{\mathrm{N}};$$

$$\int_F s^+(p_T - p_F) q_F = 0, \qquad \text{for each } T \in \mathcal{T}_h, F \in \mathcal{F}_T^{\mathrm{D}}.$$

Accordingly, the intermediate state at each $F \in \mathcal{F}_T^{\mathrm{i}} \cap \mathcal{F}_{T'}^{\mathrm{i}}$ is the weighted average between the two neighbour element (T, T') states, *i.e.*,

$$\begin{aligned} \boldsymbol{\pi}_F^k \left((s^+ - s^-)\boldsymbol{u}_F \right) &= \boldsymbol{\pi}_F^k \left(s^+ \boldsymbol{u}_T - s^- \boldsymbol{u}_{T'} \right), \\ \pi_F^k \left((s^+ - s^-)p_F \right) &= \pi_F^k \left(s^+ p_T - s^- p_{T'} \right). \end{aligned} \tag{24}$$

The `HHO-HLL` formulation falls into the generalized framework of Riemann solvers for hybrid DG methods proposed by Vila-Pérez *et al.*[51] and is based on the Exact Riemann Solver (ERS) for variable density incompressible flows devised in [49]. In particular, following [53], the ERS based HLL Riemann solver can be derived: the flux$_\star$ in the *star* region delimited by the two external acoustic waves reads

$$\begin{aligned} (\boldsymbol{u} \otimes \boldsymbol{u} + p\boldsymbol{I})_\star \cdot \boldsymbol{n}_{FT} &= \frac{s_{T'} (\boldsymbol{u}_T \otimes \boldsymbol{u}_T + p_T \boldsymbol{I}) - s_T (\boldsymbol{u}_{T'} \otimes \boldsymbol{u}_{T'} + p_{T'} \boldsymbol{I})}{s_{T'} - s_T} \cdot \boldsymbol{n}_{FT} \\ &\quad + \frac{s_{T'} s_T}{s_{T'} - s_T} (\boldsymbol{u}_{T'} - \boldsymbol{u}_T), \\ (\boldsymbol{u})_\star \cdot \boldsymbol{n}_{FT} &= \frac{s_{T'} \boldsymbol{u}_T - s_T \boldsymbol{u}_{T'}}{s_{T'} - s_T} \cdot \boldsymbol{n}_{FT} + \frac{s_{T'} s_T}{s_{T'} - s_T} \frac{1}{a^2} (p_{T'} - p_T). \end{aligned}$$

The two external acoustic wave speeds are

$$\begin{aligned} s_{T'} &= \frac{1}{2} \left(\boldsymbol{u}_{T'} \cdot \boldsymbol{n}_{TF} + \sqrt{(\boldsymbol{u}_{T'} \cdot \boldsymbol{n}_{TF})^2 + 4a^2} \right), \\ s_T &= \frac{1}{2} \left(\boldsymbol{u}_T \cdot \boldsymbol{n}_{TF} - \sqrt{(\boldsymbol{u}_T \cdot \boldsymbol{n}_{TF})^2 + 4a^2} \right), \end{aligned}$$

regardless of the compressive or expansive nature of the acoustic waves, see Appendix B4 in [49] for details. Defining the intermediate state as

$$\boldsymbol{u}_F = \frac{s_{T'} \boldsymbol{u}_T - s_T \boldsymbol{u}_{T'}}{s_{T'} - s_T} \qquad \text{and} \qquad p_F = \frac{s_{T'} p_T - s_T p_{T'}}{s_{T'} - s_T},$$

and performing some trivial algebraic manipulations, the flux$_\star$ can be written as follows

$$(\boldsymbol{u} \otimes \boldsymbol{u} + p\boldsymbol{I})_\star \cdot \boldsymbol{n}_{FT} = (\boldsymbol{u}_F \otimes \boldsymbol{u}_T + p_F\boldsymbol{I}) \cdot \boldsymbol{n}_{FT} + s_{T'}(\boldsymbol{u}_T - \boldsymbol{u}_F)$$
$$- \frac{s_T}{s_{T'} - s_T}\boldsymbol{u}_{T'}\left[(\boldsymbol{u}_{T'} - \boldsymbol{u}_T) \cdot \boldsymbol{n}_{TF}\right],$$
$$(\boldsymbol{u})_\star \cdot \boldsymbol{n}_{FT} = \boldsymbol{u}_F \cdot \boldsymbol{n}_{FT} + s_{T'}\frac{1}{a^2}(p_T - p_F).$$

In order to decouple neighboring elements, the continuity of the normal component of the velocity is assumed by hypothesis, namely $\boldsymbol{u}_T \cdot \boldsymbol{n}_{TF} = \boldsymbol{u}_{T'} \cdot \boldsymbol{n}_{TF} = \boldsymbol{u}_F \cdot \boldsymbol{n}_{TF}$. Thus, the numerical fluxes in Equations (22)-(23) as well as the interface conditions in (24) and the wave speeds in (19) are directly obtained. We remark that, according to the HLL machinery, see [53] for details, unique definition of numerical fluxes follows from the observation that $s_{T'} > 0$ and $s_T < 0$.

3 Numerical Results

We open the section discussing the numerical setup of test cases presented in what follows, in particular we briefly mention about numerical integration, basis function and solution strategy choices.

We consider computational meshes composed of triangular and quadrilateral mesh elements and line segment mesh faces. Numerical integration over mesh elements and mesh faces is performed over standardized polygons of reference (reference triangle and reference square) and over the standardized segment, respectively, based on Gaussian quadrature rules. Reference-to-physical-frame mappings from reference entities to mesh entities are defined by means of Lagrange polynomials. Discrete polynomial spaces over mesh elements and mesh faces are spanned by orthonormal modal bases. Since all the computational meshes considered in this work feature affine reference-to-physical frame mappings, note that bilinear trapezoidal elements are avoided, the exact same accuracy can be obtained using either reference or physical frame basis functions, see [54] for details. That being said, our preferred setup, in the context of HHO formulations, consist in relying upon physical frame polynomial spaces over mesh elements and reference frame polynomial spaces over mesh faces, as proposed in [55]. Orthogonalization in the physical frame is performed element-by-element starting from a monomial basis defined in a local reference frame aligned with the principal axes of inertia of each mesh element, as described in [25].

Steady state numerical solutions are sought by means of pseudo-transient continuation, an established Newton's method globalization strategy [56]. Unsteady computations are advanced in time by means of a second-order accurate backward differentiation formula. At each time step the nonlinear equations system is solved using Newton's method, see for example [57]. At each Newton iteration the linearised equations system is solved using the LU factorization implementation provided by the Intel oneAPI Math Kernel Library (oneMKL). We remark that static condensation is performed element-by-element during matrix assembly in order to reduce the dimension of the global system matrix, accordingly the LU factorization is applied to the statically condensed equations system. Our computational framework allows to perform matrix assembly and static condensation in parallel based on a shared memory paradigm. In this work solely unsteady computations are run in parallel. We mention that also oneMKL is multithreaded.

3.1 Kovasznay Flow

Steady flow behind a grid made of equally spaced parallel rods is described by the following exact solution of the incompressible Navier–Stokes equations (see [58])

$$
\begin{aligned}
\boldsymbol{u} &= \left[1 - e^{\kappa x} \cos\left(2\pi y\right)\right] \boldsymbol{i} + \frac{\kappa}{2\pi} e^{\kappa x} \sin\left(2\pi y\right) \boldsymbol{j}, \\
p &= p_0 - \frac{1}{2} e^{2\kappa x},
\end{aligned}
\tag{25}
$$

where $p_0 \in \mathbb{R}$ is an arbitrary constant and the parameter κ depends on the Reynolds number

$$
\kappa = \frac{\mathrm{Re}}{2} - \sqrt{\frac{\mathrm{Re}^2}{4} + 4\pi^2}.
$$

The Kovasznay flow problem is defined on the bi-unit square computational domain $\Omega = (-0.5, 1.5) \times (0, 2)$ and solved by means of the `HHO-Hdiv` and `HHO-HLL` schemes. Boundary conditions are derived from the Kovasznay analytical solution (25) at $\mathrm{Re} = \frac{1}{\nu} = 40$. In particular, a Neumann boundary condition is imposed at the outflow boundary (right side of the square domain) while Dirichlet boundary conditions are imposed on the remaining boundaries.

In order to numerically validate the proposed HHO schemes, we consider h-refined mesh sequences composed of regular triangular and quadrilateral elements, and several polynomial degrees $k = \{1, 2, 3, 4\}$. Quadrilateral elements meshes are obtained doubling the number of mesh elements in each Cartesian direction at each refinement step, while triangular elements meshes are obtained by means of the Delaunay algorithm. For the triangular elements mesh sequence the four fold increase of the mesh cardinality is approximately replicated. Errors in L^2-norm and h-convergence rates are tabulated for the approximated pressure, divergence of the velocity, velocity, and velocity gradients fields. Results over triangular elements meshes are reported in Tables 2 and 3 for `HHO-Hdiv` and `HHO-HLL` schemes, respectively. Results over quadrilateral elements meshes are reported in Tables 4 and 5 for `HHO-Hdiv` and `HHO-HLL` schemes, respectively. As a general observation it can be noticed that, although the level of accuracy provided by the two schemes proposed is comparable, the `HHO-Hdiv` scheme takes the lead over triangular elements meshes while `HHO-HLL` is to be preferred over quadrilateral meshes.

Since the flow is diffusion dominated at this Reynolds number, the `HHO-HLL` scheme shows an asymptotic convergence rate of $k+2$ for the velocity and $k+1$ for pressure, velocity divergence and velocity gradients. The convergence rates obtained over quadrilateral elements meshes are slightly better than those on triangular elements meshes, at all polynomial degrees. Notice that, at the same mesh sequence refinement step, quadrilateral meshes have twice the number of elements as compared to triangular meshes.

`HHO-Hdiv` scheme shows asymptotic convergence rates of order $k + 1$ for the pressure unknown on both triangular and quadrilateral meshes. The incompressibility constraint is exactly satisfied, note that the velocity divergence errors settle around the machine precision. Convergence rates for the velocity and the velocity gradients differs when applying `HHO-Hdiv` on triangular and quadrilateral elements meshes. On triangular meshes we observe the optimal rates of $k + 2$ and $k + 1$ for the velocity and the velocity gradients, respectively, while on quadrilateral meshes the convergence tops at $k+1$ and k, respectively. Accordingly, a full order of convergence is lost. We refer to the work of Kirk *et al.* [40] for additional clues regarding improved convergence rates on simplexes.

As remarked in Sect. 2.4.2, we verify that optimal convergence rates on quadrilateral meshes can be recovered by lowering the degree of polynomials employed to approximate the numerical trace of the pressure on mesh faces. Results for the `HHO-DivFree` scheme on the quadrilateral mesh sequence are reported in Table 6. Since the `HHO-DivFree` scheme is not H-div conforming and has demonstrated to be less robust than `HHO-HLL` in convection-dominated flow regimes, it will not be further investigated in subsequent test cases.

In order to provide a baseline for evaluating the accuracy of HHO formulations in the diffusion dominated flow regime, we numerically solve the Kovasznay test case by means of the Discontinuos Galerkin formulation proposed and analysed by Di Pietro and Ern [23], here denoted with the acronym `DG-SkewSymm`. Similarly to the `HHO-Hdiv` formulation, `DG-SkewSymm` employs a skew-symmetric trilinear convective term discretization and is kinetic energy preserving. The pressure-velocity coupling formulation can be traced back to the approach proposed in [18], where Riemann solvers for the artificial-compressibility perturbation of the Stokes and Navier-Stokes problems were derived and employed for handling numerical fluxes on the mesh skeleton. The viscous term discretization is based on the Bassi-Rebay BR2 formulation [16]. We remark that, also a DG discretization based the HLL flux of `HHO-HLL` has been implemented and tested. Nevertheless, since the numerical results are comparable with those of `DG-SkewSymm`, we decided to favor the scheme for whom rigorous theoretical analysis is available.

The numerical results over triangular and quadrilateral mesh sequences, reported in Tables 7 and 8, respectively, confirm the error analysis results of [23]: order $k + 1$ is observed for the velocity error in L^2 norm and order k is attained for both the pressure error and the velocity gradient error in L^2 norm. For the sake of comparison we consider the same polynomial degrees and mesh sequences employed for `HHO-Hdiv` and `HHO-HLL`. Indeed, in what follows, we consider the polynomial degree leading the dimension of the Jacobian matrix and the size of Jacobian matrix blocks as a reference to compare the convergence rates. We remind that, in case of DG, k is the degree of polynomial spaces in d variables defined over mesh elements. We remark that in case of HHO, thanks to static condensation, only the polynomial degree of polynomial spaces defined over mesh faces influences the size of the global matrix.

Comparing Tables 3–7 and 5–8, it can be appreciated that `HHO-HLL` improves `DG-SkewSymm` convergence rates by one order over triangular and quadrilateral mesh sequences, for both velocity, pressure and velocity gradients. L^2 errors of HHO formulations are smaller on coarse meshes and approximately one order of magnitude tinier on fine meshes, thanks to the improved rate of convergence. `HHO-Hdiv` provides better results than `HHO-HLL` on triangular meshes, accordingly, both HHO formulations are able to improve DG results on simplexes. As opposite, since `HHO-Hdiv` loses superconvergence on quadrilateral meshes, it is possible to appreciate that the velocity error levels are on pair with those of `DG-SkewSymm`, see Tables 4–8. Nevertheless, we remark that pressure errors provided by `HHO-Hdiv` are better than those of `HHO-HLL` and up to two orders of magnitude smaller than those of `DG-SkewSymm` on fine meshes, over both triangular and quadrilateral mesh sequences. This latter observations suggests that a divergence-free velocity field is beneficial in terms of pressure accuracy.

3.2 LLMS Pressure Gradient Test Case

In order to investigate pressure-robustness, *i.e.,* velocity solution accuracy in the presence of strong pressure gradients [39, 59], we consider the test case proposed by Lederer, Linke, Mer-

Table 2 Kovasznay flow. Errors and h-convergence rates for the HHO$-$Hdiv scheme on the triangular elements mesh sequence

	card($\mathcal{T}_h$)	$\|\nabla \boldsymbol{u}_T - \nabla \boldsymbol{u}\|_{L^2}$	Order	$\|\boldsymbol{u}_T - \boldsymbol{u}\|_{L^2}$	Order	$\|p_T - p\|_{L^2}$	Order	$\|\nabla \cdot \boldsymbol{u}_T\|_{L^2}$	Order
$k = 1$	50	2.45e+00	–	1.07e-01	–	6.94e-02	–	5.57e-16	–
	192	8.86e-01	1.51	2.30e-02	2.29	1.87e-02	1.95	5.32e-16	–
	810	2.99e-01	1.51	3.62e-03	2.57	4.99e-03	1.83	5.16e-16	–
	3126	8.50e-02	1.86	4.93e-04	2.95	1.18e-03	2.14	5.04e-16	–
	12706	2.28e-02	1.88	6.64e-05	2.86	2.87e-04	2.01	5.05e-16	–
$k = 2$	50	9.01e-01	–	3.30e-02	–	1.85e-02	–	8.67e-16	–
	192	1.61e-01	2.56	2.62e-03	3.77	1.58e-03	3.66	5.97e-16	–
	810	2.33e-02	2.69	1.72e-04	3.78	1.98e-04	2.89	5.05e-16	–
	3126	3.80e-03	2.68	1.47e-05	3.64	2.74e-05	2.93	5.52e-16	–
	12706	4.75e-04	2.97	8.98e-07	3.99	3.08e-06	3.12	5.58e-16	–
$k = 3$	50	1.94e-01	–	4.26e-03	–	2.26e-03	–	6.99e-16	–
	192	2.10e-02	3.31	2.44e-04	4.25	1.78e-04	3.78	6.90e-16	–
	810	1.83e-03	3.39	1.02e-05	4.42	1.23e-05	3.71	5.96e-16	–
	3126	1.24e-04	3.99	3.43e-07	5.02	6.67e-07	4.31	5.90e-16	–
	12706	8.14e-06	3.88	1.12e-08	4.88	4.05e-08	4.00	5.92e-16	–
$k = 4$	50	4.44e-02	–	8.93e-04	–	3.98e-04	–	8.21e-16	–
	192	2.02e-03	4.60	1.99e-05	5.66	1.15e-05	5.26	6.42e-16	–
	810	7.67e-05	4.54	3.18e-07	5.74	3.65e-07	4.80	5.94e-16	–
	3126	3.32e-06	4.65	7.32e-09	5.59	1.35e-08	4.89	6.22e-16	–
	12706	9.90e-08	5.01	1.05e-10	6.05	3.84e-10	5.07	6.29e-16	–

Table 3 Kovasznay flow. Errors and h-convergence rates for the HHO–HLL scheme on the triangular element mesh sequence

	card($\mathcal{T}_h$)	$\|\nabla \boldsymbol{u}_T - \nabla \boldsymbol{u}\|_{L^2}$	Order	$\|\boldsymbol{u}_T - \boldsymbol{u}\|_{L^2}$	Order	$\|p_T - p\|_{L^2}$	Order	$\|\nabla \cdot \boldsymbol{u}_T\|_{L^2}$	Order
$k=1$	50	3.22e+00	–	3.30e-01	–	2.38e-01	–	4.80e-01	–
	192	1.46e+00	1.18	7.54e-02	2.20	4.70e-02	2.41	3.62e-01	0.42
	810	5.23e-01	1.43	1.30e-02	2.44	7.56e-03	2.54	1.42e-01	1.30
	3126	1.66e-01	1.70	1.89e-03	2.85	1.38e-03	2.52	5.36e-02	1.44
	12706	4.76e-02	1.78	2.66e-04	2.80	2.65e-04	2.35	1.75e-02	1.60
$k=2$	50	1.37e+00	–	8.12e-02	–	6.24e-02	–	2.65e-01	–
	192	2.10e-01	2.79	7.22e-03	3.60	4.67e-03	3.85	4.87e-02	2.52
	810	3.20e-02	2.62	4.95e-04	3.72	3.83e-04	3.47	8.45e-03	2.43
	3126	5.29e-03	2.67	4.32e-05	3.61	5.34e-05	2.92	1.47e-03	2.59
	12706	7.22e-04	2.84	2.97e-06	3.82	6.94e-06	2.91	2.21e-04	2.70
$k=3$	50	2.22e-01	–	1.06e-02	–	3.99e-03	–	3.97e-02	–
	192	2.23e-02	3.42	5.15e-04	4.49	2.70e-04	4.00	4.93e-03	3.10
	810	1.96e-03	3.38	2.41e-05	4.26	1.95e-05	3.65	4.63e-04	3.28
	3126	1.44e-04	3.86	8.77e-07	4.91	1.41e-06	3.90	4.01e-05	3.62
	12706	9.91e-06	3.82	3.08e-08	4.78	9.03e-08	3.92	2.95e-06	3.72
$k=4$	50	4.44e-02	–	1.63e-03	–	1.10e-03	–	1.14e-02	–
	192	1.78e-03	4.78	3.24e-05	5.83	2.27e-05	5.77	4.42e-04	4.83
	810	6.99e-05	4.50	6.46e-07	5.44	8.01e-07	4.65	1.93e-05	4.35
	3126	3.02e-06	4.65	1.47e-08	5.61	3.12e-08	4.80	8.39e-07	4.64
	12706	1.05e-07	4.79	2.62e-10	5.74	1.09e-09	4.79	3.07e-08	4.72

Table 4 Kovasznay flow. Errors and h-convergence rates for the $\mathrm{HHO-H\dot{d}iv}$ scheme on the quadrilateral elements mesh sequence

	card($\mathcal{T}_h$)	$\|\nabla \boldsymbol{u}_T - \nabla \boldsymbol{u}\|_{L^2}$	Order	$\|\boldsymbol{u}_T - \boldsymbol{u}\|_{L^2}$	Order	$\|p_T - p\|_{L^2}$	Order	$\|\nabla \cdot \boldsymbol{u}_T\|_{L^2}$	Order
$k=1$	64	4.01e+00	–	1.40e-01	–	2.93e-02	–	3.91e-16	–
	256	1.99e+00	1.01	3.53e-02	1.99	7.96e-03	1.88	3.14e-16	–
	1024	9.90e-01	1.00	8.97e-03	1.98	2.27e-03	1.81	3.18e-16	–
	4096	4.94e-01	1.00	2.26e-03	1.99	5.98e-04	1.93	2.79e-16	–
	16384	2.47e-01	1.00	5.67e-04	1.99	1.52e-04	1.97	3.04e-16	–
$k=2$	64	8.88e-01	–	1.96e-02	–	4.01e-03	–	3.12e-16	–
	256	2.15e-01	2.05	2.33e-03	3.07	3.31e-04	3.60	3.67e-16	–
	1024	5.32e-02	2.01	2.84e-04	3.04	2.36e-05	3.81	3.42e-16	–
	4096	1.33e-02	2.00	3.52e-05	3.01	1.78e-06	3.73	3.34e-16	–
	16384	3.31e-03	2.00	4.39e-06	3.00	1.59e-07	3.49	3.75e-16	–
$k=3$	64	1.26e-01	–	1.82e-03	–	2.67e-04	–	3.32e-16	–
	256	1.53e-02	3.04	1.15e-04	3.98	2.29e-05	3.54	3.63e-16	–
	1024	1.90e-03	3.01	7.22e-06	3.99	1.57e-06	3.87	3.60e-16	–
	4096	2.36e-04	3.00	4.52e-07	4.00	1.00e-07	3.97	3.39e-16	–
	16384	2.95e-05	3.00	2.83e-08	4.00	6.31e-09	3.99	3.70e-16	–
$k=4$	64	1.35e-02	–	1.46e-04	–	2.12e-05	–	3.29e-16	–
	256	8.16e-04	4.05	4.32e-06	5.08	4.33e-07	5.61	3.67e-16	–
	1024	5.04e-05	4.02	1.32e-07	5.03	8.65e-09	5.64	4.06e-16	–
	4096	3.14e-06	4.00	4.11e-09	5.01	2.00e-10	5.44	3.94e-16	–
	16384	1.96e-07	4.00	1.28e-10	5.00	5.40e-12	5.21	4.30e-16	–

Table 5 Kovasznay flow. Errors and h–convergence rates for the HHO–HLL scheme on the quadrilateral elements mesh sequence

	card($\mathcal{T}_h$)	$\|\nabla\boldsymbol{u}_T - \nabla\boldsymbol{u}\|_{L^2}$	Order	$\|\boldsymbol{u}_T - \boldsymbol{u}\|_{L^2}$	Order	$\|p_T - p\|_{L^2}$	Order	$\|\nabla\cdot\boldsymbol{u}_T\|_{L^2}$	Order
$k=1$	64	2.11e+00	–	1.08e-01	–	7.82e-02	–	1.38e-01	–
	256	7.63e-01	1.47	1.67e-02	2.70	1.20e-02	2.70	8.86e-02	0.64
	1024	2.45e-01	1.64	2.69e-03	2.63	1.97e-03	2.61	3.44e-02	1.36
	4096	7.19e-02	1.77	4.12e-04	2.71	3.11e-04	2.66	1.07e-02	1.68
	16384	1.97e-02	1.87	5.82e-05	2.82	5.08e-05	2.62	2.99e-03	1.84
$k=2$	64	3.42e-01	–	1.39e-02	–	6.62e-03	–	3.70e-02	–
	256	5.94e-02	2.53	1.28e-03	3.44	7.09e-04	3.22	7.78e-03	2.25
	1024	9.17e-03	2.69	9.73e-05	3.72	5.73e-05	3.63	1.39e-03	2.48
	4096	1.29e-03	2.83	6.77e-06	3.85	5.61e-06	3.35	2.13e-04	2.71
	16384	1.73e-04	2.91	4.48e-07	3.92	6.49e-07	3.11	2.97e-05	2.84
$k=3$	64	4.17e-02	–	1.23e-03	–	5.86e-04	–	7.60e-03	–
	256	3.25e-03	3.68	5.05e-05	4.60	2.54e-05	4.53	7.69e-04	3.30
	1024	2.35e-04	3.79	1.92e-06	4.72	1.28e-06	4.32	6.43e-05	3.58
	4096	1.61e-05	3.86	6.73e-08	4.84	5.72e-08	4.48	4.85e-06	3.73
	16384	1.06e-06	3.92	2.24e-09	4.91	2.66e-09	4.42	3.38e-07	3.84
$k=4$	64	3.73e-03	–	8.16e-05	–	4.07e-05	–	5.57e-04	–
	256	1.49e-04	4.64	1.59e-06	5.69	1.12e-06	5.19	2.01e-05	4.79
	1024	5.38e-06	4.80	2.80e-08	5.82	3.29e-08	5.09	7.31e-07	4.78
	4096	1.81e-07	4.89	4.67e-10	5.91	9.85e-10	5.06	2.57e-08	4.83
	16384	5.91e-09	4.94	7.56e-12	5.95	2.97e-11	5.05	8.95e-10	4.84

Table 6 Kovasznay flow. Errors and h-convergence rates for the HHO-DivFree scheme on the quadrilateral elements mesh sequence

	card($\mathcal{T}_h$)	$\|\nabla \boldsymbol{u}_T - \nabla \boldsymbol{u}\|_{L^2}$	Order	$\|\boldsymbol{u}_T - \boldsymbol{u}\|_{L^2}$	Order	$\|p_T - p\|_{L^2}$	Order	$\|\nabla \cdot \boldsymbol{u}_T\|_{L^2}$	Order
$k = 1$	64	1.26e+00	–	5.65e-02	–	2.11e-02	–	1.73e-16	–
	256	3.07e-01	2.04	6.25e-03	3.18	2.33e-03	3.18	2.23e-16	–
	1024	7.63e-02	2.01	7.80e-04	3.00	5.17e-04	2.17	2.92e-16	–
	4096	1.91e-02	2.00	9.83e-05	2.99	1.28e-04	2.02	3.31e-16	–
	16384	4.79e-03	2.00	1.24e-05	2.99	3.19e-05	2.00	3.17e-16	–
$k = 2$	64	2.63e-01	–	6.64e-03	–	2.03e-03	–	2.02e-16	–
	256	3.46e-02	2.93	4.53e-04	3.87	1.78e-04	3.51	2.72e-16	–
	1024	4.42e-03	2.97	2.91e-05	3.96	1.42e-05	3.65	2.95e-16	–
	4096	5.58e-04	2.98	1.84e-06	3.98	1.26e-06	3.49	3.69e-16	–
	16384	7.02e-05	2.99	1.16e-07	3.99	1.32e-07	3.26	3.44e-16	–
$k = 3$	64	3.93e-02	–	6.28e-04	–	1.58e-04	–	1.97e-16	–
	256	2.64e-03	3.90	2.07e-05	4.93	4.46e-06	5.15	2.92e-16	–
	1024	1.70e-04	3.96	6.67e-07	4.95	1.79e-07	4.64	3.40e-16	–
	4096	1.08e-05	3.98	2.11e-08	4.98	7.91e-09	4.50	3.86e-16	–
	16384	6.77e-07	3.99	6.65e-10	4.99	3.64e-10	4.44	3.71e-16	–
$k = 4$	64	4.43e-03	–	5.07e-05	–	1.05e-05	–	2.39e-16	–
	256	1.49e-04	4.90	8.67e-07	5.87	2.61e-07	5.33	3.05e-16	–
	1024	4.76e-06	4.96	1.40e-08	5.96	6.45e-09	5.34	3.49e-16	–
	4096	1.50e-07	4.98	2.21e-10	5.98	1.76e-10	5.20	4.14e-16	–
	16384	4.73e-09	4.99	3.48e-12	5.99	5.13e-12	5.10	3.98e-16	–

Table 7 Kovasznay flow. Errors and h-convergence rates for the DG–SkewSymm scheme on the triangular elements mesh sequence

	card($\mathcal{T}_h$)	$\|\nabla \boldsymbol{u}_T - \nabla \boldsymbol{u}\|_{L^2}$	Order	$\|\boldsymbol{u}_T - \boldsymbol{u}\|_{L^2}$	Order	$\|p_T - p\|_{L^2}$	Order	$\|\nabla \cdot \boldsymbol{u}_T\|_{L^2}$	Order
$k = 1$	50	4.79e+00	–	3.47e-01	–	2.72e-01	–	3.95e-01	–
	192	2.70e+00	0.85	1.12e-01	1.67	8.04e-02	1.81	2.49e-01	0.69
	810	1.32e+00	1.00	2.87e-02	1.90	2.92e-02	1.41	1.08e-01	1.16
	3126	6.57e-01	1.03	7.12e-03	2.06	1.22e-02	1.29	4.73e-02	1.23
	12706	3.25e-01	1.00	1.81e-03	1.96	5.59e-03	1.12	2.21e-02	1.09
$k = 2$	50	1.88e+00	–	9.10e-02	–	6.33e-02	–	2.33e-01	–
	192	4.63e-01	2.09	1.22e-02	2.99	9.96e-03	2.75	5.75e-02	2.08
	810	1.11e-01	1.98	1.39e-03	3.01	1.73e-03	2.43	1.24e-02	2.13
	3126	2.99e-02	1.94	1.96e-04	2.90	4.32e-04	2.06	3.04e-03	2.08
	12706	7.18e-03	2.03	2.37e-05	3.01	1.03e-04	2.04	7.33e-04	2.03
$k = 3$	50	4.28e-01	–	1.73e-02	–	7.00e-03	–	3.44e-02	–
	192	5.61e-02	3.02	1.09e-03	4.10	9.01e-04	3.05	6.48e-03	2.48
	810	7.11e-03	2.87	7.67e-05	3.69	1.12e-04	2.89	7.91e-04	2.92
	3126	8.94e-04	3.07	4.81e-06	4.10	1.42e-05	3.06	1.07e-04	2.97
	12706	1.09e-04	3.00	2.96e-07	3.98	1.68e-06	3.05	1.24e-05	3.07
$k = 4$	50	7.78e-02	–	2.32e-03	–	1.93e-03	–	1.27e-02	–
	192	5.12e-03	4.05	7.86e-05	5.03	8.32e-05	4.68	6.91e-04	4.33
	810	3.20e-04	3.85	2.64e-06	4.72	5.05e-06	3.89	4.25e-05	3.87
	3126	2.28e-05	3.91	9.90e-08	4.86	3.44e-07	3.98	2.70e-06	4.08
	12706	1.38e-06	3.99	3.08e-09	4.95	2.16e-08	3.94	1.70e-07	3.94

Table 8 Kovasznay flow. Errors and h-convergence rates for the DG–SkewSymm scheme on the quadrilateral elements mesh sequence

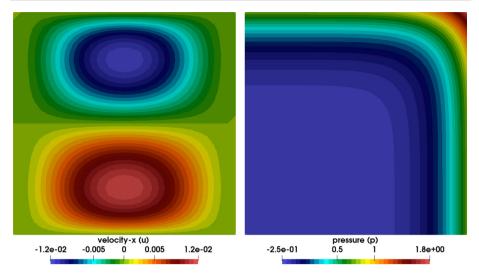|	card($\mathcal{T}_h$)	$\|\nabla \boldsymbol{u}_T - \nabla \boldsymbol{u}\|_{L^2}$	Order	$\|\boldsymbol{u}_T - \boldsymbol{u}\|_{L^2}$	Order	$\|p_T - p\|_{L^2}$	Order	$\|\nabla \cdot \boldsymbol{u}_T\|_{L^2}$	Order
$k = 1$	64	3.33e+00	–	1.39e-01	–	7.54e-02	–	8.24e-02	–
	256	1.70e+00	0.97	3.79e-02	1.87	2.92e-02	1.37	2.45e-02	1.75
	1024	8.51e-01	1.00	9.75e-03	1.96	1.19e-02	1.30	6.65e-03	1.88
	4096	4.26e-01	1.00	2.50e-03	1.96	5.50e-03	1.11	1.71e-03	1.96
	16384	2.13e-01	1.00	6.38e-04	1.97	2.68e-03	1.04	4.43e-04	1.95
$k = 2$	64	7.27e-01	–	2.09e-02	–	7.71e-03	–	4.50e-02	–
	256	1.84e-01	1.99	2.59e-03	3.01	1.96e-03	1.97	1.13e-02	1.99
	1024	4.59e-02	2.00	3.22e-04	3.01	4.89e-04	2.00	2.90e-03	1.97
	4096	1.15e-02	2.00	4.01e-05	3.01	1.22e-04	2.01	7.31e-04	1.99
	16384	2.87e-03	2.00	5.01e-06	3.00	3.02e-05	2.01	1.83e-04	2.00
$k = 3$	64	1.04e-01	–	2.29e-03	–	1.52e-03	–	1.22e-02	–
	256	1.32e-02	2.98	1.52e-04	3.91	1.60e-04	3.25	1.58e-03	2.95
	1024	1.64e-03	3.00	9.77e-06	3.96	1.82e-05	3.13	1.92e-04	3.04
	4096	2.05e-04	3.00	6.19e-07	3.98	2.18e-06	3.06	2.36e-05	3.02
	16384	2.56e-05	3.00	3.89e-08	3.99	2.67e-07	3.03	2.93e-06	3.01
$k = 4$	64	1.17e-02	–	1.86e-04	–	1.56e-04	–	1.60e-03	–
	256	7.50e-04	3.96	5.78e-06	5.01	1.14e-05	3.78	8.68e-05	4.20
	1024	4.71e-05	3.99	1.79e-07	5.01	7.64e-07	3.90	4.90e-06	4.15
	4096	2.94e-06	4.00	5.57e-09	5.01	4.85e-08	3.98	2.92e-07	4.07
	16384	1.84e-07	4.00	1.74e-10	5.00	3.04e-09	4.00	1.79e-08	4.03

Fig. 1 LLMS pressure gradient. Horizontal velocity component (u) and pressure (p) fields ($p_0 = -0.25$)

don and Schöberl (LLMS) [59], hereinafter referred to as LLMS pressure gradient test case. We impose boundary conditions and forcing term $\boldsymbol{f}$ according to the following analytical velocity and pressure fields

$$\boldsymbol{u} = \nabla \times \zeta \qquad \text{and} \qquad p = p_0 + x^7 + y^7,$$

with arbitrary $p_0 \in \mathbb{R}$ and $\zeta = x^2 (x-1)^2 y^2 (y-1)^2$. In case of `HHO-Hdiv` we impose Dirichlet boundary conditions on all but one side of the unit square domain $\Omega = (0,1) \times (0,1)$, where a Neumann boundary is set. In order to ensure stability in the inviscid limit, in case of `HHO-HLL` we impose both Dirichlet and Neumann boundary conditions on all sides, leading to the so called *given* boundary conditions. We remark that, according to given BCs, HLL Riemann problems on boundary faces utilize both the analytical pressure and velocity solutions for the definition of external boundary states. We also remark that, in the context of real-life applications involving the Euler equations, suitable external states should be defined on boundary faces. The approach can be borrowed from DG methods based on Godunov fluxes, where external states on boundary elements are usually computed based on the method of characteristics, see *e.g.,* [60,Chapter 19], exploiting the hyperbolic nature of the artificial compressibility perturbation of the Euler equation.

Figure 1 shows the horizontal velocity component ($\boldsymbol{u} \cdot \boldsymbol{i}$) and pressure behavior over the computational domain. Notice the presence of a strong pressure gradient near the top-right corner of the square.

In order to numerically validate convergence rates in the diffusion dominated and convection dominated flow regimes we consider $\nu = 1$ and $\nu = 10^{-4}$, respectively. The computational domain is discretized by means of increasingly fine regular triangular elements meshes, doubling the number of elements in each Cartesian direction at each refinement step, and we focus on $k = 3$ HHO formulations. We remark that triangles are obtained by cutting square elements in two halves. Tables 9-12 summarize the convergence analysis considering errors in L^2-norm for the velocity, the velocity gradients and the pressure fields. In the diffusion dominated regime both `HHO-Hdiv` and `HHO-HLL` deliver the same convergence rates, *i.e.,* order $k + 2$ for the velocity and $k + 1$ for pressure and velocity gradients. In the

Table 9 LLMS pressure gradient. Errors and h-convergence rates for $k = 3$ HHO-Hdiv with $\nu = 1$

card($\mathcal{T}_h$)	$\|\nabla \boldsymbol{u}_T - \nabla \boldsymbol{u}\|_{L^2}$	Order	$\|\boldsymbol{u}_T - \boldsymbol{u}\|_{L^2}$	Order	$\|p_T - p\|_{L^2}$	Order
32	7.22e-04	–	1.02e-05	–	3.07e-04	–
128	5.34e-05	3.76	4.05e-07	4.65	1.93e-05	3.99
512	3.60e-06	3.89	1.43e-08	4.82	1.18e-06	4.03
2048	2.34e-07	3.94	4.74e-10	4.91	7.20e-08	4.03
8192	1.49e-08	3.97	1.53E-11	4.95	4.43e-09	4.02

Table 10 LLMS pressure gradient. Errors and h-convergence rates for $k = 3$ HHO-HLL with $\nu = 1$

card($\mathcal{T}_h$)	$\|\nabla \boldsymbol{u}_T - \nabla \boldsymbol{u}\|_{L^2}$	Order	$\|\boldsymbol{u}_T - \boldsymbol{u}\|_{L^2}$	Order	$\|p_T - p\|_{L^2}$	Order
32	4.59e-04	–	1.14e-05	–	4.50e-04	–
128	2.85e-05	4.01	3.63e-07	4.97	2.94e-05	3.94
512	1.72e-06	4.05	1.14e-08	4.99	1.86e-06	3.98
2048	1.04e-07	4.05	3.59e-10	4.99	1.16e-07	4.00
8192	6.41e-09	4.02	1.13e-11	4.99	7.23e-09	4.00

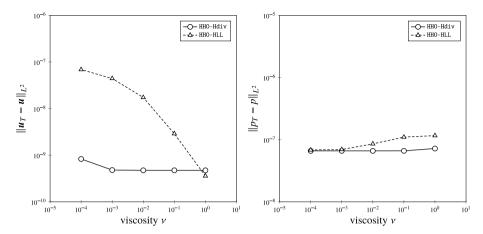**Table 11** LLMS pressure gradient. Errors and h-convergence rates for $k = 3$ HHO-Hdiv with $\nu = 10^{-4}$

card($\mathcal{T}_h$)	$\|\nabla \boldsymbol{u}_T - \nabla \boldsymbol{u}\|_{L^2}$	Order	$\|\boldsymbol{u}_T - \boldsymbol{u}\|_{L^2}$	Order	$\|p_T - p\|_{L^2}$	Order
32	1.59e-03	–	1.86e-05	–	2.58e-04	–
128	8.18e-05	4.28	5.51e-07	5.08	1.67e-05	3.95
512	6.62e-06	3.63	2.28e-08	4.59	1.05e-06	3.99
2048	4.72e-07	3.81	8.30e-10	4.78	6.60e-08	3.99
8192	3.09e-08	3.93	2.75e-11	4.92	4.13e-09	4.00

Table 12 LLMS pressure gradient. Errors and h-convergence rates for $k = 3$ HHO-HLL with $\nu = 10^{-4}$

card($\mathcal{T}_h$)	$\|\nabla \boldsymbol{u}_T - \nabla \boldsymbol{u}\|_{L^2}$	Order	$\|\boldsymbol{u}_T - \boldsymbol{u}\|_{L^2}$	Order	$\|p_T - p\|_{L^2}$	Order
32	2.15e-02	–	5.77e-04	–	2.65e-04	–
128	2.22e-03	3.28	2.45e-05	4.56	1.72e-05	3.95
512	2.50e-04	3.15	1.24e-06	4.30	1.09e-06	3.98
2048	2.88e-05	3.12	6.85e-08	4.18	6.82e-08	4.00
8192	3.24e-06	3.15	3.88e-09	4.14	4.27e-09	4.00

convection dominated regime, only HHO-Hdiv maintains the aforementioned convergence rates, while the HHO-HLL scheme loses an order on velocity and velocity gradients fields.

Figure 2 depicts the pressure and velocity errors in L^2-norm over the 2k triangular elements mesh for different viscosities values, *i.e.,* $\nu = \{1, 10^{-1}, 10^{-2}, 10^{-3}, 10^{-4}\}$. The fact that velocity errors are almost unaltered while varying the viscosity confirms that the HHO-Hdiv formulation is pressure-robust. Note that the velocity errors provided by the HHO-HLL scheme increase by two orders of magnitude while decreasing the viscosity by four orders of magnitude.

Fig. 2 LLMS pressure gradient. $k = 3$ `HHO-Hdiv` and `HHO-HLL` formulations on a 2048 triangular elements mesh. *Left and right*: Velocity and pressure errors in L^2-norm, respectively, while changing the viscosity (ν)
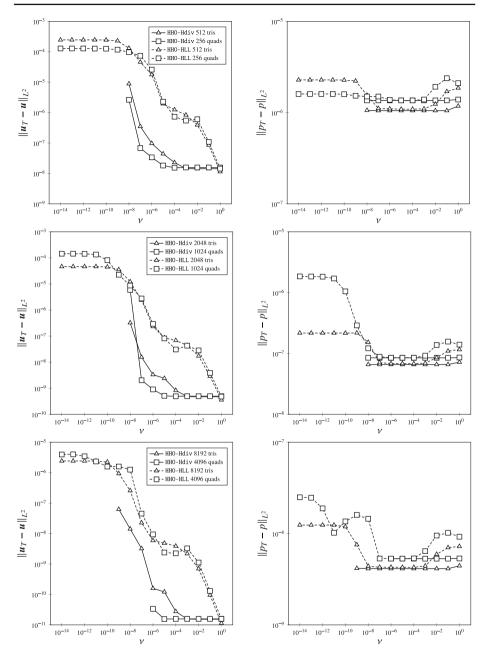
We next investigate robustness in the inviscid limit considering $k = 3$ and $k = 4$ HHO formulations over triangular and quadrilateral meshes and varying the viscosity in one order of magnitude steps from 1 to 10^{-14}. The error analysis reported in Figs. 3 and 4 for different mesh densities, see figures captions for details, shows that pressure-robustness does not guarantee robustness in the inviscid limit. Indeed, only the `HHO-HLL` formulation is stable in the limit of vanishing viscosity. The velocity errors provided by the `HHO-Hdiv` formulation tend to dramatically increase for $\nu < 10^{-5}$. Moreover, due to convergence failure of Newton's method globalization strategy [56], the numerical solutions are not available for $\nu < 10^{-7}$. We verified that even using the L^2-projection of the exact solution as initial guess the simulation blows up. Interestingly, the `HHO-HLL` formulation shows to be resilient in the inviscid limit: notice that the velocity error reaches a plateau while decreasing the viscosity below 10^{-10} and also the pressure error is well behaved. In case of $k = 4$ `HHO-HLL` formulations over the 8k triangular and the 4k quadrilateral mesh, the velocity errors increase by three orders of magnitude moving from the diffusion dominated regime to the inviscid limit, while the pressure error stays almost constant around 10^{-11}.
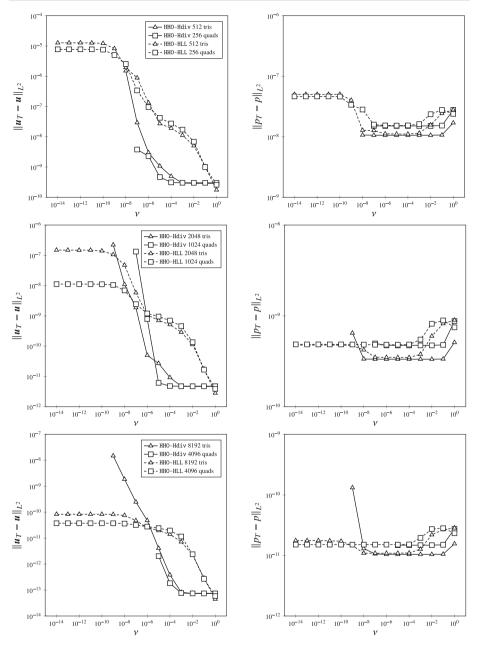
3.3 Gresho-Chan Vortex

Originally proposed by Gresho & Chan [61], who named it 'triangular vortex', this viscous 2D model problem is designed to study the schemes capability of preserving vortical structures. Our analysis relies on the numerical set-up described by Gauger *et al.*[62]: time integration is carried out over a double periodic unit squared domain $\Omega = (0, 1) \times (0, 1)$ based on the following initial conditions

$$(u, v, p) = (u_0, v_0, p_0) + \begin{cases} \left(-5\widetilde{y}, \; 5\widetilde{x}, \; \dfrac{25}{2}r^2 \right), & \text{if } 0 \le r < 0.2, \\[2ex] \left(-2\dfrac{\widetilde{y}}{r} + 5\widetilde{y}, \; 2\dfrac{\widetilde{x}}{r} - 5\widetilde{x}, \; 4\ln 5r + \dfrac{25}{2}r^2 - 20r + 4 \right), & \text{if } 0.2 \le r < 0.4, \\[2ex] \left(0, \; 0, \; 4\ln 2 - 2 \right), & \text{if } 0.4 \le r; \end{cases}$$

Fig. 3 LLMS pressure gradient. Robustness in the inviscid limit, $k = 3$ `HHO-Hdiv` (solid lines) and `HHO-HLL` (dashed lines) formulations. *Left and right*: velocity and pressure error in L^2-norm, respectively. In each row, from top to bottom, increasingly dense triangular (triangular marks) and quadrilateral (square marks) meshes are considered
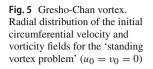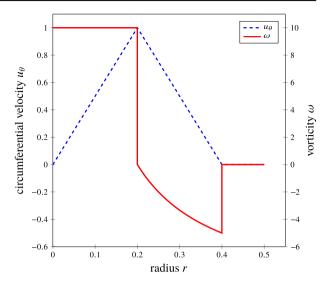
Fig. 4 LLMS pressure gradient. Robustness in the inviscid limit, $k = 4$ HHO-Hdiv (solid lines) and HHO-HLL (dashed lines) formulations. *Left and right*: velocity and pressure error in L^2-norm, respectively. In each row, from top to bottom, increasingly dense triangular (triangular marks) and quadrilateral (square marks) meshes are considered

Fig. 5 Gresho-Chan vortex. Radial distribution of the initial circumferential velocity and vorticity fields for the 'standing vortex problem' ($u_0 = v_0 = 0$)

where u_0, v_0, p_0 are user-defined real parameters. Notice that a local coordinate system $\widetilde{x} = x - x_0$ is employed to define the radial distance $r = (\widetilde{x}^2 + \widetilde{y}^2)^{0.5}$ from the vortex center $x_0 = [0.5 \ 0.5]^{\mathsf{T}}$ at the initial simulation time.

Figure 5 shows the initial circumferential velocity u_θ and vorticity $\omega = \nabla \times u$ fields as function of the radial distance from the vortex center in case of a 'standing vortex problem', i.e., $u_0 = v_0 = 0$. Notice the peculiar triangular distribution of the circumferential velocity, from whom the test name originates. Interestingly, the velocity field yields a discontinuous vorticity field: a rigid body rotation core ($r < 0.2$) with constant counter-clockwise vorticity comes in contact with an annular region ($0.2 \leq r < 0.4$) with radially increasing clockwise vorticity followed by an external region ($0.4 \leq r$) with fluid at rest (null vorticity).
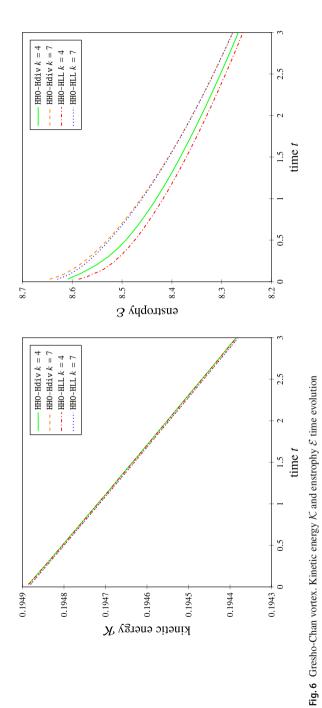
The numerical investigation is performed imposing $u_0 = v_0 = 1/3$ (moving vortex), $p_0 = 0$ and setting the viscosity as $\nu = 10^{-5}$. BDF2 implicit time integration [63] with a constant step size $\Delta t = t_F/10^4$ is adopted to advance the solution up to the dimensionless end time $t_F = 3$, resulting in the simulation of one period of the moving vortex.

We consider $k = 4$ and $k = 7$ HHO-Hdiv and HHO-HLL formulations on a regular 32×32 quadrilateral elements mesh. The higher polynomial degree is considered as a reference to evaluate the behavior of the lowest order discretization with respect to the evolution of kinetic energy $\mathcal{K}$ and enstrophy $\mathcal{E}$, defined as follows
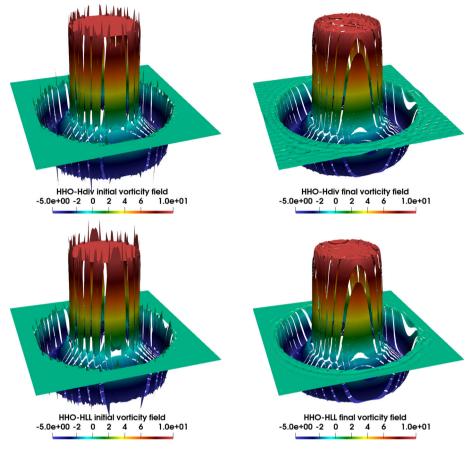
$$\mathcal{K} = \frac{1}{2} \int_\Omega u \cdot u, \qquad \mathcal{E} = \frac{1}{2} \int_\Omega \omega \cdot \omega.$$

All the simulations performed provide an accurate picture of kinetic energy evolution, see Fig. 6. Notice in particular that the kinetic energy decays are superimposed for both schemes and both polynomial degrees. Some differences might be appreciated in terms of enstrophy behavior: while the HHO-HLL and HHO-Hdiv curves are almost superimposed at $k = 7$, at $k = 4$ the HHO-HLL scheme underestimates the enstrophy by a more significant amount.

Figure 7 depicts the vorticity fields at the initial and final simulation times. Because of the discontinuous nature of the initial vorticity field, local over/under-shoots are present at initialization, nonetheless, the final solution looks smoother and the vortex is well resolved. The results suggest that both schemes are capable of satisfactorily preserving vortical struc-

Fig. 6 Gresho-Chan vortex. Kinetic energy $\mathcal{K}$ and enstrophy $\mathcal{E}$ time evolution

Fig. 7 Gresho-Chan vortex. Vorticity fields (color coded and warped by vorticity magnitude) at $k = 4$. *Left and right*: initial and final simulation times, respectively. *Top and bottom*: HHO-Hdiv and HHO-HLL schemes, respectively

tures. Note however that HHO-Hdiv shows some high-frequency oscillations that are absent in the final HHO-Hdiv solution.

3.4 Double Shear Layer

The double shear layer problem devised by Bell *et al.*[64] focuses on inviscid ($\nu = 0$) unsteady flow modelling capabilities. Time integration is performed over a double periodic unit square domain $\Omega = (0, 1) \times (0, 1)$ by means of the BDF2 scheme. The initial horizontal and vertical velocity components are set as

$$ u = \begin{cases} \tanh\left(\dfrac{y - 0.25}{\xi}\right) & y \leq 0.5 \\ \tanh\left(\dfrac{0.75 - y}{\xi}\right) & y > 0.5 \end{cases}, \quad \text{and} \quad v = \delta \sin\left(2\pi x\right), $$
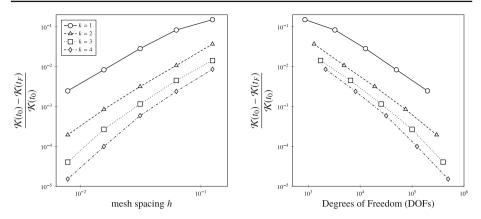
Fig. 8 Double shear layer. `HHO-HLL` kinetic energy relative error at the final time. *Left and right*: in dependence of the mesh spacing and of the DOFs of the discretized system, respectively

respectively. The pressure field is uniform and the free parameters are set as $\xi = 1/30$ and $\delta = 1/20$.

We consider $k = \{1, 2, 3, 4\}$ `HHO-HLL` formulations on a h-refined regular quadrilateral elements mesh sequence such that $\text{card}(\mathcal{T}_h) = 64 * 4^i$, $i = 0, 1, 2, 3, 4$. Time integration is carried out in the time interval $(t_0 = 0, t_F = 2]$ utilizing a constant time step $\Delta t = 10^{-3}$. Upon time integration completion, the relative kinetic energy error, defined as

$$\frac{\mathcal{K}(t_0) - \mathcal{K}(t_F)}{\mathcal{K}(t_0)},$$

is a measure of the amount of numerical dissipation introduced by the scheme. Due to its lack of robustness in the inviscid limit, `HHO-Hdiv` fails to complete the test case, regardless of the polynomial degree and the mesh density, the simulation blows up at early stages. Accordingly only `HHO-HLL` results are presented hereafter.

In Fig. 8 the relative kinetic energy error is plotted against mesh spacing and DOFs. As expected, finer meshes and higher polynomial degrees provide increasingly small numerical dissipation. Moreover, increasing the polynomial degree is always beneficial in terms of error versus DOFs. Considering the finest two grids of the h-refined mesh sequence, the kinetic energy error convergence rates are $\{1.76, 2.13, 2.73, 2.71\}$ for $k = \{1, 2, 3, 4\}$, respectively. Probably, due to the high accuracy required to capture all the flow features, finer meshes and smaller time-steps would be required to reach asymptotic convergence rates. Indeed, as depicted in Fig. 9 in case of $k = 4$ `HHO-HLL` formulations, only the finest mesh allows to satisfactorily represent the tiniest vortical features. This behaviour testifies about the challenges involved in the simulation of the double shear layer.

3.5 Lid-driven Cavity Flow

We consider the well-known lid-driven cavity flow problem over a unit square domain $\Omega = (0, 1) \times (0, 1)$ at Reynolds $\text{Re} = \frac{1}{\nu} = 10^4$. Dirichlet boundary conditions are imposed on the sliding top wall and the remaining stationary walls. In order to evaluate the robustness of HHO formulations with respect to the mesh distortion we consider a 12768 triangular elements mesh featuring anisotropic and stretched simplexes, see Fig. 10. $k = 4$ `HHO-HLL`
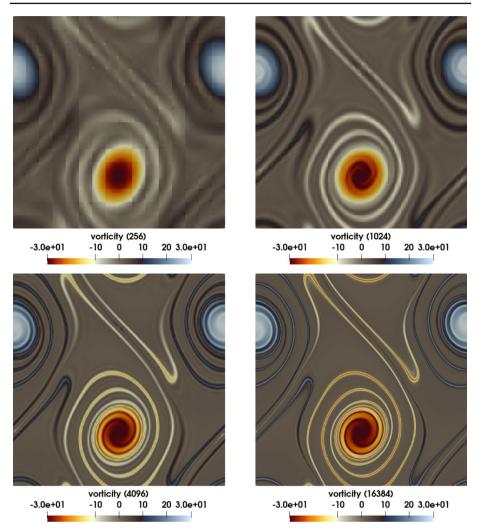
Fig. 9 Double shear layer. Vorticity field at the final time obtained with $k = 4$ HHO-HLL. The mesh cardinality, *i.e.,* 256, 1024, 4096 and 16384 elements, is reported within round brackets

and HHO-Hdiv discretizations are applied for seeking steady state solutions starting from fluid at rest.

In Fig. 11 the horizontal (u) and vertical (v) velocity components are plotted along vertical ($y = 0.5$) and horizontal ($x = 0.5$) centerlines of the cavity, respectively. The two HHO formulation provide perfectly superimposed velocity profiles and are in very good agreement with reference solutions available from the literature [65, 66].

For the sake of comparison, in Fig. 12 we report the warp of the velocity magnitude fields obtained with HHO-Hdiv and HHO-HLL. It is interesting to remark that the most noticeable difference between the two numerical solutions is related to the behavior at the top-left and top-right corners of the cavity, where the velocity is discontinuous and the pressure gradient is steeper. In particular, at the top-left corner, the HHO-Hdiv velocity solution shows a less good agreement with the weakly imposed no-slip boundary condition.
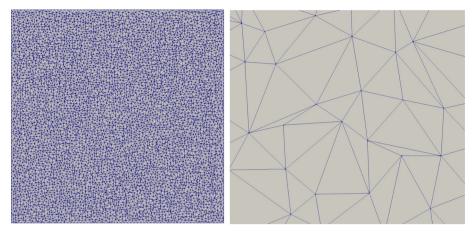
Fig. 10 Lid-driven cavity. Computational mesh. *Left and right*: global and detailed views, respectively
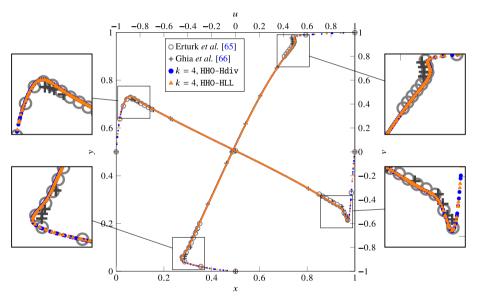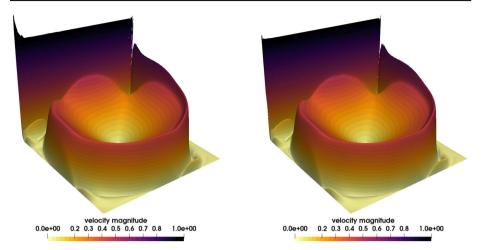

Fig. 11 Lid-driven cavity at Re $= 10k$. Comparison with reference solutions based on horizontal and vertical velocity profiles over vertical and horizontal centerlines, respectively

4 Conclusions

We numerically validated two original Hybrid High-Order formulations designed for seeking approximate solutions of incompressible flow problems. The formulations allows to cope with Dirichlet and Neumann boundary conditions and, in particular, Dirichlet boundary conditions can be imposed weakly. Pressure-robustness and robustness in the inviscid limit are investigated performing especially conceived test cases. The `HHO-HLL` scheme, thanks to the introduction of Godunov fluxes based on HLL Riemann Solvers, can be employed for seeking approximate solution of the incompressible Euler equations. The `HHO-Hdiv` scheme is pressure-robust, kinetic energy preserving and yields mass conservation up to

Fig. 12 Lid-driven cavity at Re $= 10k$. Warp of the velocity magnitude field. *Left and right*: `HHO-Hdiv` and `HHO-HLL` formulation, respectively

machine precision but is not stable in the inviscid limit. Robustness with respect to mesh distortion and grading is demonstrated for both formulations by solving the lid-driven cavity problem at high-Reynolds number over randomly distorted triangular elements meshes. The choice between `HHO-Hdiv` and `HHO-HLL` might be driven by the targeted flow regime: `HHO-Hdiv` is best suited for low-to-moderate Reynolds number flows, thanks to pressure robustness and exact mass conservation, while `HHO-HLL` is able to cope with moderate-to-high Reynolds number flows, hence rivaling DG discretizations based on Godunov fluxes.

If h-convergence rates are provided in terms of k, that is the degree of polynomial spaces leading the dimension of the Jacobian matrix and the size of Jacobian matrix blocks, both HHO formulations provide improved convergence rates with respect to state-of-the-art discontinuous Galerkin discretizations. Let's consider a d-dimensional problem, since velocity is a vector unknown and pressure is a scalar unknown, it is reasonable to associate k with the degree of polynomial spaces employed for the discretization of the velocity unknown. In case of DG, k is the degree of polynomial spaces in d variables defined over mesh elements and convergence rates of order $k + 1$ and k, respectively, are typically expected for the velocity and pressure error in L^2 norm. In the context of HHO discretizations, thanks to static condensation, elemental unknowns can be eliminated from the global matrix and the problem can be reformulated in terms of skeletal DOFs. Accordingly, k is the degree of polynomial spaces in $d - 1$ variables defined over mesh faces. The convergence rates of HHO discretizations are as follows:

  i) both `HHO-HLL` and `HHO-Hdiv` provide $k+1$ h-convergence rates for the pressure error in L^2 norm;
 ii) in the diffusion dominated flow regime, `HHO-HLL` provides $k + 2$ h-convergence rates for the velocity error in L^2 norm;
iii) at both low and moderately-high Reynolds numbers over triangular mesh sequences, `HHO-Hdiv` provides $k + 2$ h-convergence rates for the velocity error in L^2 norm, optimal convergence is lost on general meshes.

The preliminary comparison proposed in this work based on the Kovasznay test case suggest that significant gains can be expected in terms of pressure accuracy. The advantages in terms

of velocity accuracy are promising but require a more systematic comparison considering additional test cases and diverse flow regimes.

Besides convergence rates, the Jacobian matrix dimension and sparsity favors HHO discretizations over DG formulations when increasing the polynomial degree k. Comparing d and $d - 1$ variables polynomial spaces, it is clear that the dimension of the latter grows a slower pace with respect to k. This observation suggests that matrix-vector products evaluations required by iterative solution strategies are less expensive in case of high-order HHO formulations. We mention that this advantage is downturned by the cost of static condensation and back solving, that is reverting the static condensation back, which is happening at each Newton iterations in case of nonlinear problems. The comparison of p-multilevel solution strategies for HHO and DG formulations of the Stokes problem proposed in [67] provides additional clue in this regard.

While in this work we focused on 2D test cases, the formulations are well suited to be applied in 3D. Future works tackling 3D computations will require further research efforts for improving the efficiency of the solution strategy. Indeed, while 2D computations can be effectively carried out relying on direct solvers, state-of-the-art preconditioned iterative solvers are required for tackling h-refined 3D mesh sequences. A more comprehensive comparison between HHO and DG formulations for incompressible flow problems, encompassing both accuracy and computational expense, is also planned.

Data Availability Data will be made available from the corresponding author on reasonable request.

Declarations

Conflict of interest The authors declare that they have no conflict of interest.

References

1. Botti, M., Di Pietro, D.A., Sochala, P.: A hybrid high-order method for nonlinear elasticity. SIAM J. Numer. Anal. **55**(6), 2687–2717 (2017). https://doi.org/10.1137/16M1105943
2. Abbas, M., Ern, A., Pignet, N.: Hybrid high-order methods for finite deformations of hyperelastic materials. Comput. Mech. **62**(4), 909–928 (2018). https://doi.org/10.1007/s00466-018-1538-0
3. Aghili, J., Boyaval, S., Di Pietro, D.A.: Hybridization of mixed high-order methods on general meshes and application to the Stokes equations. Comput. Meth. Appl. Mat. **15**(2), 111–134 (2015). https://doi.org/10.1515/cmam-2015-0004
4. Di Pietro, D.A., Ern, A., Lemaire, S.: A review of Hybrid High-Order methods: formulations, computational aspects, comparison with other methods. Building bridges: Connections and challenges in modern

approaches to numerical partial differential equations, vol. No 114 in Lecture Notes in Computational Science and Engineering. Springer, Cham (2016) https://doi.org/10.1007/978-3-319-41640-3

5. Botti, L., Di Pietro, D.A., Droniou, J.: A hybrid high-order discretisation of the Brinkman problem robust in the Darcy and Stokes limits. Comput. Methods Appl. Mech. Engrg. **341**, 278–310 (2018). https://doi.org/10.1016/j.cma.2018.07.004

6. Botti, L., Botti, M., Di Pietro, D.A.: An abstract analysis framework for monolithic discretisations of poroelasticity with application to Hybrid High-Order methods. Comput. Math. Appl. 91, 150–175 (2021). Robust and Reliable Finite Element Methods in Poromechanics https://doi.org/10.1016/j.camwa.2020.06.004

7. Botti, L., Botti, M., Di Pietro, D.A.: A Hybrid High-Order Method for Multiple-Network Poroelasticity, pp. 227–258. Springer, Cham (2021). https://doi.org/10.1007/978-3-030-69363-3_6

8. Botti, L., Di Pietro, D.A.: p-multilevel preconditioners for HHO discretizations of the stokes equations with static condensation. Commun. Appl. Math. Comput. (2021). https://doi.org/10.1007/s42967-021-00142-5

9. Badia, S., Droniou, J., Yemm, L.: Conditioning of a Hybrid High-Order scheme on meshes with small faces. arXiv preprint (2021)

10. Cockburn, B., Shu, C.-W.: The Runge-Kutta local projection P^1-discontinuous-Galerkin finite element method for scalar conservation laws. RAIRO Modél. Math. Anal. Numér. **25**(3), 337–361 (1991). https://doi.org/10.1051/m2an/1991250303371

11. Cockburn, B., Shu, C.-W.: TVB Runge-Kutta local projection discontinuous Galerkin finite element method for conservation laws. II. General framework. Math. Comp. **52**(186), 411–435 (1989). https://doi.org/10.2307/2008474

12. Cockburn, B., Lin, S.Y., Shu, C.-W.: TVB Runge-Kutta local projection discontinuous Galerkin finite element method for conservation laws. III. One-dimensional systems. J. Comput. Phys. **84**(1), 90–113 (1989). https://doi.org/10.1016/0021-9991(89)90183-6

13. Cockburn, B., Hou, S., Shu, C.-W.: The Runge-Kutta local projection discontinuous Galerkin finite element method for conservation laws. IV. The multidimensional case. Math. Comp. **54**(190), 545–581 (1990). https://doi.org/10.2307/2008501

14. Cockburn, B., Shu, C.-W.: The Runge-Kutta discontinuous Galerkin method for conservation laws. V. Multidimensional systems. J. Comput. Phys. **141**(2), 199–224 (1998). https://doi.org/10.1006/jcph.1998.5892

15. Bassi, F., Rebay, S.: A high-order accurate discontinuous finite element method for the numerical solution of the compressible Navier-Stokes equations. J. Comput. Phys. **131**(2), 267–279 (1997). https://doi.org/10.1006/jcph.1996.5572

16. Bassi, F., Rebay, S., Mariotti, G., Pedinotti, S., Savini, M.: A high-order accurate discontinuous finite element method for inviscid and viscous turbomachinery flows. In: Decuypere, R., Dibelius, G. (eds.) Proceedings of the 2nd European Conference on Turbomachinery Fluid Dynamics and Thermodynamics, pp. 99–109 (1997)

17. Cockburn, B., Kanschat, G., Schötzau, D., Schwab, C.: Local discontinuous galerkin methods for the stokes system. SIAM J. Numer. Anal. **40**(1), 319–343 (2002)

18. Bassi, F., Crivellini, A., Di Pietro, D.A., Rebay, S.: An artificial compressibility flux for the discontinuous Galerkin solution of the incompressible Navier-Stokes equations. J. Comput. Phys. **218**(2), 794–815 (2006). https://doi.org/10.1016/j.jcp.2006.03.006

19. Chorin, A.J.: A numerical method for solving incompressible viscous flow problems. J. Comput. Phys. **2**(1), 12–26 (1967). https://doi.org/10.1016/0021-9991(67)90037-X

20. Shahbazi, K., Fischer, P.F., Ethier, C.R.: A high-order discontinuous Galerkin method for the unsteady incompressible Navier-Stokes equations. J. Comput. Phys. **222**(1), 391–407 (2007). https://doi.org/10.1016/j.jcp.2006.07.029

21. Botti, L., Di Pietro, D.A.: A pressure-correction scheme for convection-dominated incompressible flows with discontinuous velocity and continuous pressure. J. Comput. Phys. **230**(3), 572–585 (2011). https://doi.org/10.1016/j.jcp.2010.10.004

22. Busto, S., Ferrín, J.L., Toro, E.F., Vázquez-Cendón, M.E.: A projection hybrid high order finite volume/finite element method for incompressible turbulent flows. J. Comput. Phys. **353**, 169–192 (2018). https://doi.org/10.1016/j.jcp.2017.10.004

23. Di Pietro, D.A., Ern, A.: Discrete functional analysis tools for discontinuous Galerkin methods with application to the incompressible Navier-Stokes equations. Math. Comp. **79**(271), 1303–1330 (2010). https://doi.org/10.1090/S0025-5718-10-02333-1

24. Di Pietro, D.A., Ern, A.: Mathematical Aspects of Discontinuous Galerkin Methods. Mathématiques & Applications (Berlin) [Mathematics & Applications], vol. 69, p. 384. Springer, Heidelberg (2012). https://doi.org/10.1007/978-3-642-22980-0

25. Bassi, F., Botti, L., Colombo, A., Di Pietro, D.A., Tesini, P.: On the flexibility of agglomeration based physical space discontinuous Galerkin discretizations. J. Comput. Phys. **231**(1), 45–65 (2012). https://doi.org/10.1016/j.jcp.2011.08.018

26. Bassi, F., Botti, L., Colombo, A., Rebay, S.: Agglomeration based discontinuous Galerkin discretization of the Euler and Navier-Stokes equations. Comput. Fluids **61**, 77–85 (2012). https://doi.org/10.1016/j.compfluid.2011.11.002

27. Bassi, F., Botti, L., Colombo, A.: Agglomeration-based physical frame dG discretizations: an attempt to be mesh free. Math. Models Methods Appl. Sci. **24**(8), 1495–1539 (2014). https://doi.org/10.1142/S0218202514400028

28. Antonietti, P.F., Giani, S., Houston, P.: hp-version composite discontinuous Galerkin methods for elliptic problems on complicated domains. SIAM J. Sci. Comput. **35**(3), 1417–1439 (2013). https://doi.org/10.1137/120877246

29. Antonietti, P.F., Cangiani, A., Collis, J., Dong, Z., Georgoulis, E.H., Giani, S., Houston, P.: Review of discontinuous Galerkin finite element methods for partial differential equations on complicated domains. In: Building Bridges: Connections and Challenges in Modern Approaches to Numerical Partial Differential Equations. Lect. Notes Comput. Sci. Eng., vol. 114, pp. 279–308. Springer, Cham (2016)

30. Cangiani, A., Dong, Z., Georgoulis, E.H., Houston, P.: hp-version Discontinuous Galerkin Methods on Polygonal and Polyhedral Meshes. SpringerBriefs in Mathematics, p. 131. Springer, Cham (2017)

31. Tavelli, M., Dumbser, M.: A staggered space-time discontinuous Galerkin method for the three-dimensional incompressible Navier-Stokes equations on unstructured tetrahedral meshes. J. Comput. Phys. **319**, 294–323 (2016). https://doi.org/10.1016/j.jcp.2016.05.009

32. Tavelli, M., Dumbser, M.: A pressure-based semi-implicit space-time discontinuous Galerkin method on staggered unstructured meshes for the solution of the compressible Navier-Stokes equations at all Mach numbers. J. Comput. Phys. **341**, 341–376 (2017). https://doi.org/10.1016/j.jcp.2017.03.030

33. Dumbser, M., Fambri, F., Furci, I., Mazza, M., Serra-Capizzano, S., Tavelli, M.: Staggered discontinuous Galerkin methods for the incompressible Navier-Stokes equations: Spectral analysis and computational results. Numer. Linear Algebr. **25**(5), 2687–2717 (2018). https://doi.org/10.1002/nla.2151

34. Manzanero, J., Rubio, G., Kopriva, D.A., Ferrer, E., Valero, E.: An entropy-stable discontinuous Galerkin approximation for the incompressible Navier-Stokes equations with variable density and artificial compressibility. J. Comput. Phys. **408**, 109241 (2020). https://doi.org/10.1016/j.jcp.2020.109241

35. Nguyen, N.C., Peraire, J., Cockburn, B.: An implicit high-order hybridizable discontinuous Galerkin method for the incompressible Navier-Stokes equations. J. Comput. Phys. **230**(4), 1147–1170 (2011). https://doi.org/10.1016/j.jcp.2010.10.032

36. Cesmelioglu, A., Cockburn, B., Qiu, W.: Analysis of a hybridizable discontinuous Galerkin method for the steady-state incompressible Navier-Stokes equations. Math. Comput. **86**(306), 1643–1670 (2017). https://doi.org/10.1090/mcom/3195

37. Labeur, R.J., Wells, G.N.: Energy Stable and Momentum Conserving Hybrid Finite Element Method for the Incompressible Navier-Stokes Equations. SIAM J. Sci. Comput. **34**(2), 889–913 (2012). https://doi.org/10.1137/100818583

38. Qiu, W., Shi, K.: A superconvergent HDG method for the incompressible Navier-Stokes equations on general polyhedral meshes. IMA J. Numer. Anal. **36**(4), 1943–1967 (2016). https://doi.org/10.1093/imanum/drv067

39. Rhebergen, S., Wells, G.N.: A hybridizable discontinuous Galerkin method for the Navier-Stokes equations with pointwise divergence-free velocity field. J. Sci. Comput. **76**(3), 1484–1501 (2018). https://doi.org/10.1007/s10915-018-0671-4

40. Kirk, K.L.A., Rhebergen, S.: Analysis of a pressure-robust hybridized discontinuous galerkin method for the stationary navier-stokes equations. J. Sci. Comput. **81**(2), 881–897 (2019). https://doi.org/10.1007/s10915-019-01040-y

41. Di Pietro, D.A., Krell, S.: Benchmark session: The 2D Hybrid High-Order method. In: Cancès, C., Omnes, P. (eds.) Finite Volumes for Complex Applications VIII – Methods and Theoretical Aspects, pp. 91–106 (2017)

42. Di Pietro, D.A., Krell, S.: A hybrid high-order method for the steady incompressible navier-stokes problem. J. Sci. Comput. **74**(3), 1677–1705 (2018). https://doi.org/10.1007/s10915-017-0512-x

43. Botti, L., Di Pietro, D.A., Droniou, J.: A hybrid high-order method for the incompressible navier-stokes equations based on temam's device. J. Comput. Phys. **376**, 786–816 (2019). https://doi.org/10.1016/j.jcp.2018.10.014

44. Di Pietro, D.A., Droniou, J.: The Hybrid High-Order Method for Polytopal meshes. Modeling, Simulation and Application, vol. 19. Springer, Cham (2020). https://doi.org/10.1007/978-3-030-37203-3

45. Castanon Quiroz, D., Di Pietro, D.A.: A hybrid high-order method for the incompressible navier-stokes problem robust for large irrotational body forces. Comput. Math. Appl. **79**(9), 2655–2677 (2020). https://doi.org/10.1016/j.camwa.2019.12.005
46. Botti, Michele, Castanon Quiroz, Daniel, Di Pietro, Daniele A., Harnist, André: A hybrid high-order method for creeping flows of non-Newtonian fluids. ESAIM: M2AN 55(5), 2045–2073 (2021). https://doi.org/10.1051/m2an/2021051
47. Cockburn, B., Di Pietro, D.A., Ern, A.: Bridging the hybrid high-order and hybridizable discontinuous galerkin methods. ESAIM: M2AN **50**(3), 635–650 (2016). https://doi.org/10.1051/m2an/2015051
48. Elsworth, D.T., Toro, E.F.: Riemann solvers for solving the incompressible Navier–Stokes equations using the artificial compressibility method. Technical Report 9208, College of Aeronautics, Cranfield Institute of Technology (1992). https://dspace.lib.cranfield.ac.uk/handle/1826/240
49. Bassi, F., Massa, F., Botti, L., Colombo, A.: Artificial compressibility godunov fluxes for variable density incompressible flows. Comput. Fluids **169**, 186–200 (2018). https://doi.org/10.1016/j.compfluid.2017.09.010
50. Massa, F.C., Ostrowski, L., Bassi, F., Rohde, C.: An artificial Equation of State based Riemann solver for a discontinuous Galerkin discretization of the incompressible Navier-Stokes equations. J. Comput. Phys. **448**, 110705 (2022). https://doi.org/10.1016/j.jcp.2021.110705
51. Vila-Pérez, J., Giacomini, M., Sevilla, R., Huerta, A.: Hybridisable discontinuous galerkin formulation of compressible flows. Arch. Comput. Method E. **28**(2), 753–784 (2021). https://doi.org/10.1007/s11831-020-09508-z
52. Di Pietro, D.A., Ern, A., Lemaire, S.: An arbitrary-order and compact-stencil discretization of diffusion on general meshes based on local reconstruction operators. Comput. Meth. Appl. Mat. **14**(4), 461–472 (2014). https://doi.org/10.1515/cmam-2014-0018
53. Toro, E.F.: Riemann Solvers and Numerical Methods for Fluid Dynamics. Springer, Heidelberg. (2009). https://doi.org/10.1007/b79761
54. Botti, L.: Influence of reference-to-physical frame mappings on approximation properties of discontinuous piecewise polynomial spaces. J. Sci. Comput. **52**(3), 675–703 (2012). https://doi.org/10.1007/s10915-011-9566-3
55. Botti, L., Di Pietro, D.A.: Numerical assessment of Hybrid High-Order methods on curved meshes and comparison with discontinuous Galerkin methods. J. Comput. Phys. **370**, 58–84 (2018). https://doi.org/10.1016/j.jcp.2018.05.017
56. Kelley, C.T., Keyes, D.E.: Convergence analysis of pseudo-transient continuation. SIAM J. Numer. Anal. **35**(2), 508–523 (1998). https://doi.org/10.1137/S0036142996304796
57. Brown, P.N., Saad, Y.: Convergence theory of nonlinear newton-krylov algorithms. SIAM J. Optimiz. **4**(2), 297–330 (1994). https://doi.org/10.1137/0804017
58. Kovasznay, L.I.G.: Laminar flow behind a two-dimensional grid. Math. Proc. Cambridge **44**(1), 58–62 (1948). https://doi.org/10.1017/S0305004100023999
59. Lederer, P.L., Linke, A., Merdon, C., Schöberl, J.: Divergence-free reconstruction operators for pressure-robust stokes discretizations with continuous pressure finite elements. SIAM J. Numer. Anal. **55**(3), 1291–1314 (2017). https://doi.org/10.1137/16M1089964
60. Hirsch, C.: Numerical Computation of Internal and External Flows, Volume 2: Computational Methods for Inviscid and Viscous Flows. Wiley Series in Numerical Methods in Engineering. Wiley, England (1990)
61. Gresho, P.M., Chan, S.T.: On the theory of semi-implicit projection methods for viscous incompressible flow and its implementation via a finite element method that also introduces a nearly consistent mass matrix. Part: 2 Implementation. Int. J. Numer. Meth. Fl. **11**(5), 621–659 (1990). https://doi.org/10.1002/fld.1650110510
62. Gauger, N.R., Linke, A., Schroeder, P.W.: On high-order pressure-robust space discretisations, their advantages for incompressible high Reynolds number generalised Beltrami flows and beyond. SMAI-JCM **5**, 89–129 (2019). https://doi.org/10.5802/smai-jcm.44
63. Curtiss, C.F., Hirschfelder, J.O.: Integration of Stiff Equations. PNAS **38**(3), 235–243 (1952). https://doi.org/10.1073/pnas.38.3.235
64. Bell, J.B., Colella, P., Glaz, H.M.: A second-order projection method for the incompressible navier-stokes equations. J. Comput. Phys. **85**, 257–283 (1989). https://doi.org/10.1007/s10494-018-0005-5
65. Erturk, E., Corke, T.C., Gökçöl, C.: Numerical solutions of 2-D steady incompressible driven cavity flow at high Reynolds. Int. J. Numer. Meth. Fl. **48**, 747–774 (2005). https://doi.org/10.1002/fld.953
66. Ghia, U., Ghia, K.N., Shin, C.T.: High-re solutions for incompressible flow using the navier-stokes equations and a multigrid method. J. Comput. Phys. **48**, 387–411 (1982). https://doi.org/10.1016/0021-9991(82)90058-4

67. Botti, L., Pietro, D.A.D.: p-multilevel preconditioners for HHO discretizations of the stokes equations with static condensation. Commun. Appl. Math. Comput. (2021). https://doi.org/10.1007/s42967-021-00142-5